JACS
JOURNAL OF THE AMERICAN CHEMICAL SOCIETY

Article

pubs.acs.org/JACS

Proton Delivery and Removal in $[Ni(P^R_2N^{R'}_2)_2]^{2+}$ Hydrogen Production and Oxidation Catalysts

Molly O'Hagan, Ming-Hsun Ho, Jenny Y. Yang, Aaron M. Appel, M. Rakowski DuBois, Simone Raugei,* Wendy J. Shaw,* Daniel L. DuBois, and R. Morris Bullock

Center for Molecular Electrocatalysis, Pacific Northwest National Laboratory, P.O. Box 999, K2-57, Richland, Washington 99352, United States

Supporting Information

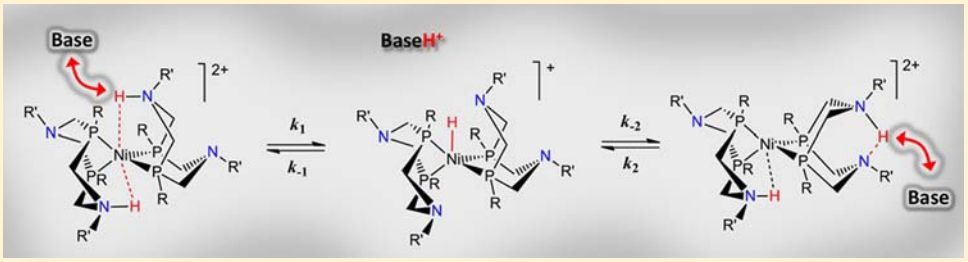

ABSTRACT: To examine the role of proton delivery and removal in the electrocatalytic oxidation and production of hydrogen by $[Ni(P^R_2N^{R'}_2)_2]^{2+}$ (where $P^R_2N^{R'}_2$ is 1,5-R′-3,7-R-1,5-diaza-3,7-diphosphacyclooctane), we report experimental and theoretical studies of the intermolecular proton exchange reactions underlying the isomerization of $[Ni(P^{Cy}_2N^{Bn}_2H)_2]^{2+}$ (Cy = cyclohexyl, Bn = benzyl) species formed during the oxidation of H_2 by $[Ni^{II}(P^{Cy}_2N^{Bn}_2)_2]^{2+}$ or the protonation of $[Ni^0(P^{Cy}_2N^{Bn}_2)_2]$. Three protonated isomers are formed (endo/endo, endo/exo, or exo/exo), which differ in the position of the N−H bond's with respect to nickel. The endo/endo isomer is the most productive isomer due to the two protons being sufficiently close to the nickel to proceed readily to the transition state to form/cleave H_2. Therefore, the rate of isomerization of the endo/exo or exo/exo isomers to generate the endo/endo isomer can have an important impact on catalytic rates. We have found that the rate of isomerization is limited by proton removal from, or delivery to, the complex. In particular, the endo position is more sterically hindered than the exo position; therefore, protonation exo to the metal is kinetically favored over endo protonation, which leads to less catalytically productive pathways. In hydrogen oxidation, deprotonation of the sterically hindered endo position by an external base may lead to slow catalytic turnover. For hydrogen production catalysts, the limited accessibility of the endo position can result in the preferential formation of the exo protonated isomers, which must undergo one or more isomerization steps to generate the catalytically productive endo protonated isomer. The results of these studies highlight the importance of precise proton delivery, and the mechanistic details described herein will be used to guide future catalyst design.

INTRODUCTION

Electrocatalysts that rapidly and efficiently interconvert electrical energy and chemical energy (bonds) will play a critical role in a secure energy future that addresses increasing worldwide energy demand and rising CO_2 emissions. H_2 production and oxidation are among the simplest reactions for energy storage. Studies of these reactions can be used to develop control over the movement of electrons and protons, which is essential for the efficient storage and utilization of energy in H_2. In biological systems, the elegantly controlled delivery and removal of protons at specific positions in the active sites of enzymes suggest that precise control of proton movement is crucial for the efficient catalytic interconversion of electrical energy and chemical bonds. For example, metalloenzymes such as hydrogenase, PSII and cytochrome *c* oxidase have highly effective proton channels that deliver and remove protons at the metal active site by precisely positioning proton acceptors/donors in a chain,[1] thereby utilizing the Grotthus mechanism of proton transfer.[2] In [FeFe]-hydrogenases, such a proton channel terminates with a pendant amine in the second coordination sphere of the active site, which in turn relays protons directly to or from the open coordination site of the iron center.[1a,3]

Using the hydrogenase enzyme active site as a model, synthetic hydrogen production/oxidation electrocatalysts have been developed, which contain pendant amines in the second coordination sphere.[4] Research in our laboratories has focused on $[Ni(P^R_2N^{R'}_2)_2]^{2+}$ (where $P^R_2N^{R'}_2$ is 1,5-R′-3,7-R-1,5-diaza-3,7-diphosphacyclooctane) catalysts containing pendant amines. These complexes and closely related analogues are the fastest synthetic catalysts known to date for hydrogen production[5] and oxidation,[6] and reversible catalysis has been demonstrated for catalysts in solution[7] and on modified

Received: July 27, 2012
Published: October 16, 2012

electrodes.[8] In the case of hydrogen production, the rates exceed those observed for the hydrogenase enzymes, although a significantly higher overpotential is required.[5] While these catalysts are fast, the measured catalytic rates for both hydrogen oxidation and production in the $[Ni(P^{R}_{2}N^{R'}_{2})_{2}]^{2+}$ systems vary significantly depending on the acids/bases used for the same catalyst.[5a,6,9] For hydrogen production catalysts, rates can increase by an order of magnitude with the use of a small acid, such as protonated dimethylformamide $[(DMF)H]^{+}$, as compared to a larger acid, such as *p*-cyanoanilinium.[5a,9] Similar effects related to the bulkiness of the base are observed for hydrogen oxidation catalysis.[10] The dependence of the catalytic rates on acid/base size suggests that the protonation site and/or the rate of proton delivery/removal changes depending on the conditions and may be limiting catalysis in some cases.

Previous investigations showed that addition of H_2 to $[Ni(P^{R}_{2}N^{R'}_{2})_{2}]^{2+}$ systems results in the reduction of Ni^{II} to Ni^{0} and protonation of the pendant amines, leading to three isomeric $[Ni(P^{R}_{2}N^{R'}_{2}H)_{2}]^{2+}$ complexes (Figure 1). These

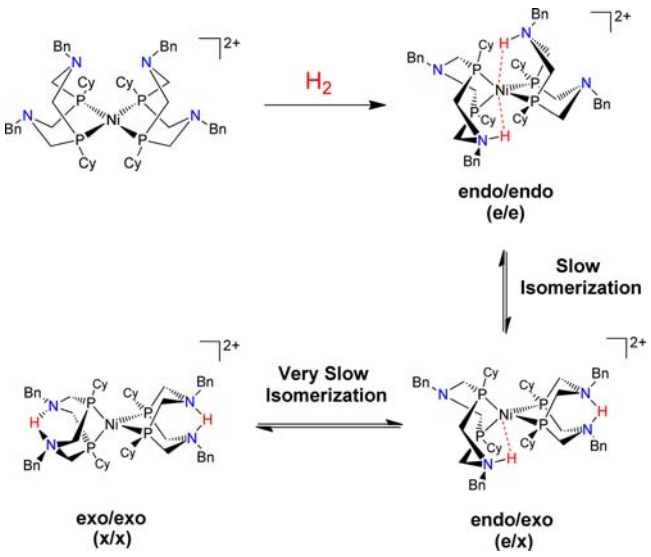

Figure 1. Structures of the endo/endo (**e**/**e**), endo/exo (**e**/**x**), and exo/exo (**x**/**x**) isomers formed by the stoichiometric reaction of $[Ni(P^{Cy}_{2}N^{Bn}_{2})_{2}]^{2+}$ with H_2, in the absence of an external base.

isomers are in equilibrium, and differ in the position of the two protons with respect to the metal.[11] The existence of these three isomers indicates that the protonated pendant amines can have distinctly different environments, and not all of these isomers are catalytically competent. The proposed catalytic intermediates of H_2 oxidation and production, including the endo/endo (**e**/**e**) isomer, are the same, as illustrated by Scheme 1, but occur in the opposite order. The positioning of the amines adjacent to nickel is essential for catalytic activity in these complexes, and it is proposed to facilitate the formation and reactivity of the proton−hydride (**e**/**NiH**) complex (Scheme 1).[12] When the six-membered ring containing the N atom of the pendant amine is properly positioned, heterolytic H−H bond cleavage/formation is facilitated by the close positioning of the nickel center, which acts as a hydride donor/acceptor, and the pendant base, which acts as a proton donor/acceptor.[12b] Exo positioned protons, as in the endo/exo (**e**/**x**) isomer and the exo/exo (**x**/**x**) isomer, are positioned incorrectly for the release of H_2.[13] It is expected that the population distribution of these three isomers and the rate of isomerization to and from the active **e**/**e** isomer will affect the observed catalytic rates.

Detailed NMR and theoretical studies of $[Ni(P^{Cy}_{2}N^{Bn}_{2}H)_{2}]^{2+}$ have shown that when the pendant amines are protonated in the endo position with respect to nickel, as shown for the **e**/**e** and **e**/**x** isomers, intramolecular proton movement between the metal center and the endo pendant amine is facile.[12c] This results in the exchange of the endo protons between the two pendant amines of the same ligand for the **e**/**e** or the **e**/**x** isomers with rate constants of about 10^{5} s^{-1} at 298 K.[12c] Therefore, intramolecular proton movement between the pendant amine and the metal center is not a rate-determining step in hydrogen oxidation with this catalyst[12c] (TOF = 10 s^{-1} at 22 °C under 1 atm H_2).[14] However, the interconversion of the different isomers and the population distribution of these isomers have not been investigated. To understand the effect that these isomers and their interconversion have upon catalysis, we have used ^{1}H and ^{31}P NMR spectroscopy studies along with computational methods to characterize the formation and interconversion of the **e**/**e**, **e**/**x**, and **x**/**x** isomers. The results of these studies have been combined to develop a mechanistic understanding of intermolecular proton transfer and how it relates to the overall catalytic cycle. This understanding will, in turn, be utilized for designing improved catalysts for H_2 production and oxidation.

RESULTS

Kinetic Products of Protonation. On the basis of kinetic studies of H_2 production catalysis,[5] we have proposed that the $[Ni(P^{R}_{2}N^{R'}_{2})_{2}]^{2+}$ catalysts are reduced and protonated twice to form $[Ni(P^{R}_{2}N^{R'}_{2}H)_{2}]^{2+}$ complexes, which exist as three isomers.[15] These are the same three isomers proposed from studies of the H_2 oxidation catalysts, as illustrated in Figure 1.[11,12c] An important unresolved question is the kinetic distribution of the isomers initially formed through protonation of the reduced complexes. Is the kinetic product of these reactions the desired **e**/**e** isomer, or are the catalytically less productive **e**/**x** and **x**/**x** isomers formed? To probe this question, we studied the protonation of $[Ni^{0}(P^{Cy}_{2}N^{Bn}_{2})_{2}]$ and $[HNi(P^{Cy}_{2}N^{Bn}_{2})_{2}]^{+}$ complexes. The $[Ni(P^{Cy}_{2}N^{Bn}_{2})_{2}]$ system, a catalyst for H_2 oxidation, was chosen because the **e**/**e**, **e**/**x**, and

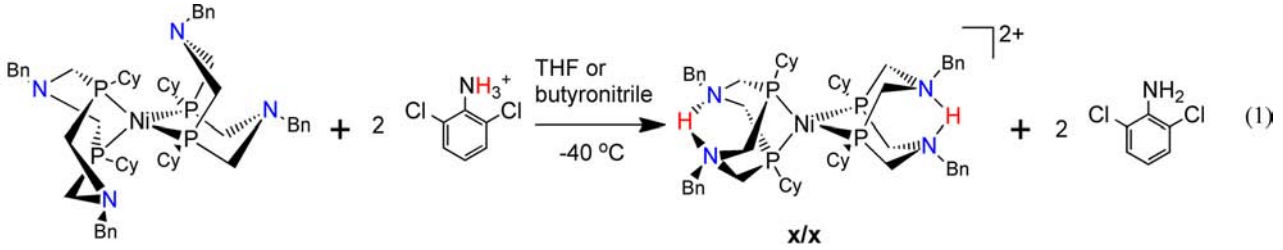

(1)

dx.doi.org/10.1021/ja307413x | J. Am. Chem. Soc. 2012, 134, 19409−19424

Scheme 1. Proposed Catalytic Cycle for H_2 Oxidation (clockwise) and H_2 Production (counterclockwise)

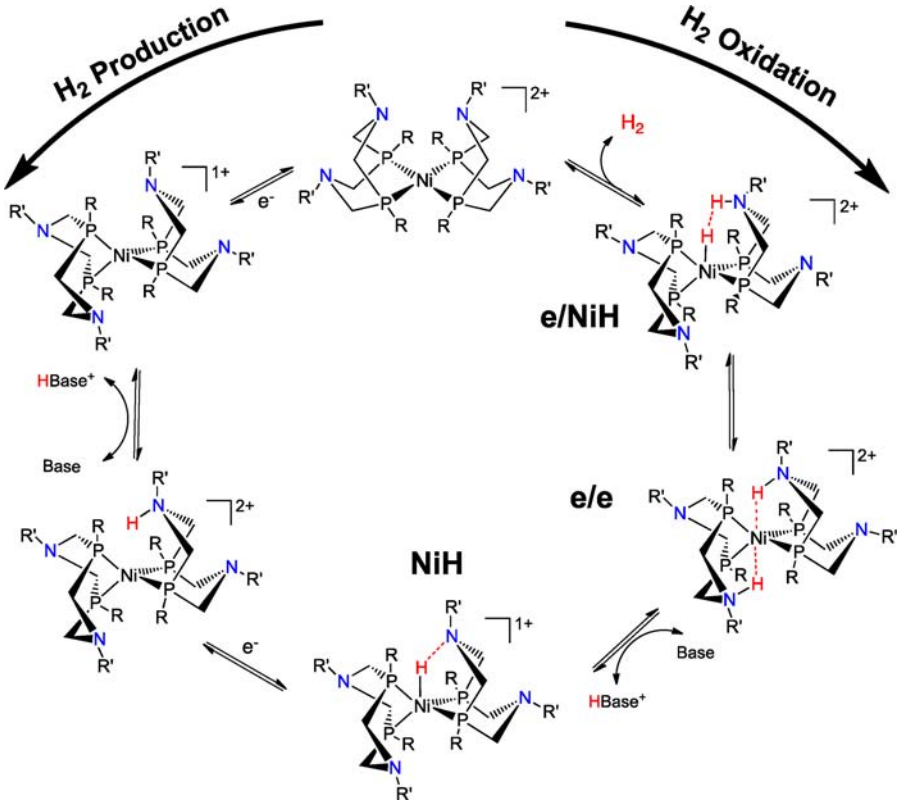

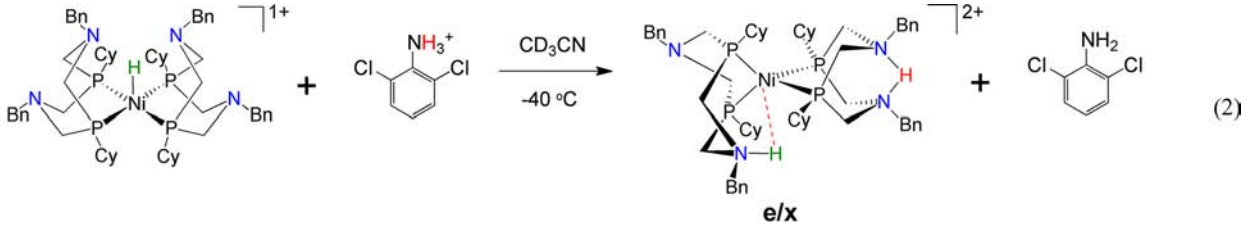

x/x isomers formed are stable against H_2 elimination, unlike H_2 production catalysts. Additionally, the *intra*molecular proton exchange pathways have been studied in detail and are well understood for this catalyst for H_2 oxidation.[12c]

The kinetic products of protonation were studied by adding two equivalents of acid to $[Ni^0(P^{Cy}_2N^{Bn}_2)_2]$ (eq 1) or one equivalent of acid to $[HNi(P^{Cy}_2N^{Bn}_2)_2]^+$ (eq 2). 2,6-dichloroanilium $[(2,6\text{-DCA})H]^+$ and $[(DMF)H]^+$ were employed as the acids since they have been used in previous studies of related hydrogen production catalysts[5a] and are sufficiently acidic (pK_a values of 5.1 and 6.1 in MeCN, respectively[16]) to irreversibly protonate both $[Ni^0(P^{Cy}_2N^{Bn}_2)_2]$ and $[HNi(P^{Cy}_2N^{Bn}_2)_2]^+$ (pK_a of the protonated pendant amine in $[Ni(P^{Cy}_2N^{Bn}_2H)_2]^{2+}$ is 13.4). The $^{31}P\{^1H\}$ NMR spectrum following the addition of $[(2,6\text{-DCA})H]^+$ to $[Ni^0(P^{Cy}_2N^{Bn}_2)_2]$ (Figure 2 and detail in the Supporting Information) showed that the **x/x** isomer was the dominant product of protonation in THF at −40 °C. These results are consistent with exo protonation being kinetically favored.

Protonation of one of the proposed catalytic intermediates, $[HNi(P^{Cy}_2N^{Bn}_2)_2]^+$ (**NiH**, Scheme 1), was also studied. Exo protonation of this nickel hydride would result in the formation of the **e/x** isomer, as the proton from the metal is expected to readily transfer to the endo position.[12c] Similarly, endo protonation would result in the **e/e** isomer. Protonation with one equivalent of $[(2,6\text{-DCA})H]^+$ in CD_3CN gives the **e/x** isomer as the dominant species, with no **e/e** isomer observed (eq 2 and Supporting Information, Figure S3).[17]

Interconversion of Isomers. Under conditions similar to those used in proton reduction catalysis to produce hydrogen, protonation at the exo position is kinetically favored, as shown by the studies of $[Ni^0(P^{Cy}_2N^{Bn}_2)_2]$ and $[HNi(P^{Cy}_2N^{Bn}_2)_2]^+$ described above. These results indicate that isomerization to the catalytically productive **e/e** isomer is necessary for the majority of the complex during catalysis and that the rate of isomerization may control the catalytic rates. The rate of interconversion of the isomers was determined by monitoring the time required for the isomers to reach equilibrium under different conditions. Equilibration was monitored using $^{31}P\{^1H\}$ NMR spectroscopy starting from the **e/e** isomer, which can be generated almost exclusively at room temperature by the addition of H_2 to $[Ni(P^{Cy}_2N^{Bn}_2)_2]^{2+}$ (Figure 3A).[11] The **e/e** isomer equilibrates to the **e/x** and **x/x** over a period of hours to days[18] (Figures 3 and 4).

The distribution of the three isomers at equilibrium is 30% **e/e**, 57% **e/x**, and 13% **x/x** (Figures 3b and 4). At room temperature in CD_3CN, the **e/e** to **e/x** equilibration is nearly complete after 10 h, at which time the **x/x** isomer begins to

dx.doi.org/10.1021/ja307413x | J. Am. Chem. Soc. 2012, 134, 19409−19424

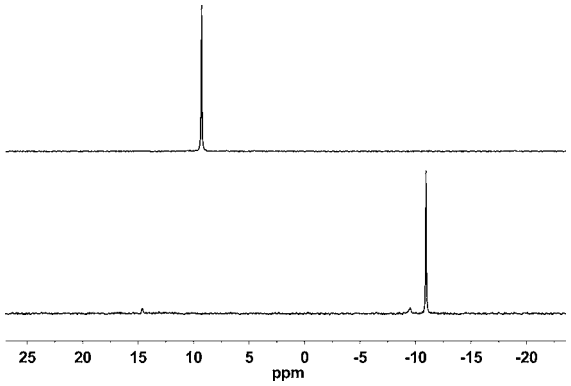

Figure 2. $^{31}P\{^{1}H\}$ NMR spectra of 20 mM $[Ni^{0}(P^{Cy}_{2}N^{Bn}_{2})_{2}]$ in THF at −40 °C (A) before protonation and (B) after the addition of two equivalents of $[(2,6\text{-DCA})H]^{+}$, showing that the **x**/**x** isomer is the major species. The * designates resonances for the **e**/**x** isomer (6%).

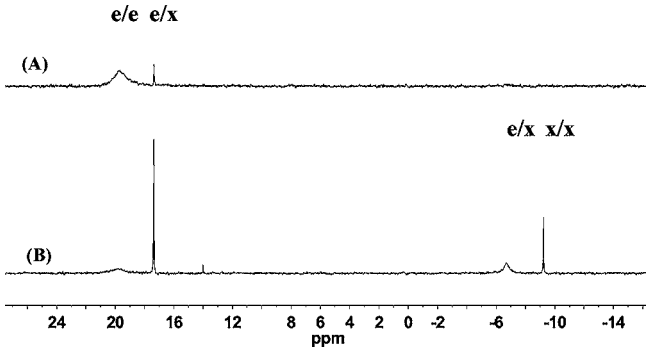

Figure 3. $^{31}P\{^{1}H\}$ NMR spectra of $[Ni(P^{Cy}_{2}N^{Bn}_{2}H)_{2}]^{2+}$ (10 mM) in CD_3CN at 298 K (A) 3 min after addition of H_2 to $[Ni(P^{Cy}_{2}N^{Bn}_{2})_{2}]^{2+}$ and (B) at equilibrium, 70 h after H_2 addition. The **e**/**e** isomer exhibits the broad resonance at 19.8 ppm; resonances at 17.4 and −6.7 ppm are due to the inequivalent phosphorus atoms of the **e**/**x** isomer; the resonance at −9.2 ppm is from the **x**/**x** isomer.[11]

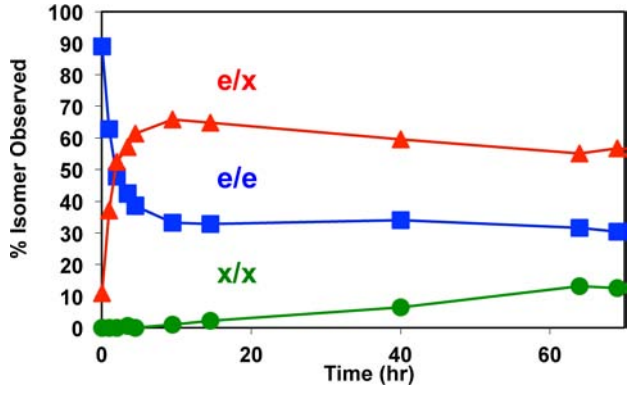

Figure 4. Isomer distribution as a function of time for 10 mM $[Ni(P^{Cy}_{2}N^{Bn}_{2}H)_{2}]^{2+}$ in CD_3CN at 22 °C. This plot shows the stepwise isomerization from the **e**/**e** isomer to the **e**/**x** isomer, then to the **x**/**x** isomer. The lines connecting data points were added for clarity.

appear. The formation of the **x**/**x** isomer is much slower, taking over 60 h to reach equilibrium (Figure 4). These findings suggest a stepwise formation of isomers, from **e**/**e** to **e**/**x**, then to **x**/**x**, where protons are sequentially transferred from the interior (endo position) to the exterior (exo position) of the complex.

The time to reach equilibrium decreases with the addition of bases, as shown in Supporting Information Figure S4. The isomerization rate increased with the strength of the base used: 2,6-DCA < DMF < aniline (pK_a of the conjugate acids being 5.1,[16a] 6.1,[16c] and 10.6[16a] respectively). The formation of the **x**/**x** isomer was ∼28 times faster in the presence of 10 equivalents of aniline compared to the rate in CD_3CN alone with no added base. It is important to note that while the isomerization *rate* increased, the isomer *distribution* was unaffected by the presence of the bases. A small amount (<3%) of the **NiH** intermediate, was observed with the addition of aniline, as illustrated in Supporting Information, Figure S5, but the ratio of **e**/**e**, **e**/**x**, and **x**/**x** was unaffected.

To examine in detail the effect of bases on isomerization, the rates of interconversion were investigated quantitatively using 2D ^{31}P NMR exchange spectroscopy experiments, EXSY, where in-phase crosspeaks are observed for nuclei undergoing chemical exchange.[19] Although DMF and 2,6-DCA were observed to increase the rate of interconversion in the equilibration studies, exchange that is rapid enough to be accessible by EXSY (ms^{-1} to s^{-1} time scales) is only observed between the **e**/**e** and **e**/**x** isomers in the presence of aniline. No exchange is observed with the **x**/**x** isomer on the EXSY time scale under any of the tested conditions.

To evaluate the mechanism of the interconversion of the **e**/**x** and **e**/**e** isomers, short mixing times were used to observe the initial step in the exchange process.[19] Both of these isomers first exhibited exchange with the **NiH** intermediate, shown in red for the **e**/**x** isomer and blue for the **e**/**e** isomer (Figure 5a and b, respectively), with the **e**/**x** isomer exchange observed earlier than the **e**/**e** isomer exchange. Only at longer mixing times were crosspeaks observed between the inequivalent ^{31}P nuclei of the endo and exo halves of the **e**/**x** isomer, shown in green, or between the **e**/**e** and **e**/**x** isomers indicated in orange (Figure 5b and c). These crosspeaks observed at longer mixing times are due to *indirect* exchange, or multiple sequential exchange processes via the **NiH** intermediate. This is further confirmed by plotting the crosspeak intensity versus the mixing time, as shown in Figure 6, where direct exchange has a nonzero initial slope and indirect exchange has an initial slope of zero.[19] Both species exhibit direct exchange with the **NiH** intermediate and indirect exchange with each other, suggesting that exchange occurs through deprotonation by the external base to generate the **NiH** intermediate as the first step in an intermolecular exchange process for both the **e**/**e** isomer and **e**/**x** isomer (Scheme 2). Deprotonation of the **e**/**x** isomer at the endo site to form a monoprotonated exo species (**x** as shown in Figure 7), was not observed experimentally and is predicted computationally to be a high energy intermediate (see below).

The exchange mechanism shown in Scheme 2 was also investigated by ^{1}H EXSY (Supporting Information, Figure S6), where exchange between the exo and aniline protons is observed before exchange of the endo and aniline protons. Exchange of the endo proton of the **e**/**x** isomer with the **NiH** intermediate is also observed before exchange with aniline. This is consistent with the **NiH** intermediate being the central species in the **e**/**e** ⇆ **e**/**x** exchange process, where removal of the exo proton by base is followed by the endo proton migrating to the metal center to form the **NiH** intermediate. Prior studies have shown that deprotonation of $[Ni(P^{Cy}_{2}N^{Bn}_{2}H)_{2}]^{2+}$ generates the **NiH** intermediate.[11,20] Quantification of the proton exchange rates using ^{1}H EXSY was not

dx.doi.org/10.1021/ja307413x | J. Am. Chem. Soc. 2012, 134, 19409−19424

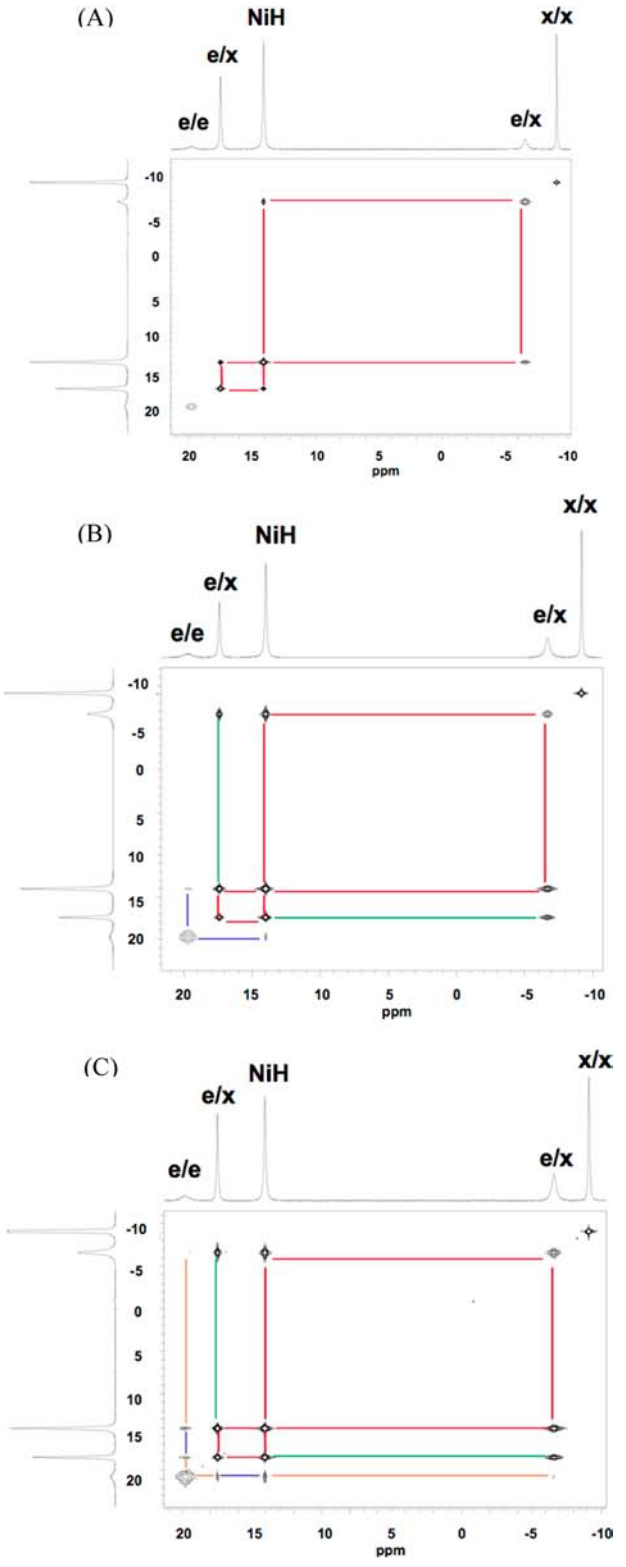

Figure 5. ^{31}P EXSY NMR spectra showing the stepwise isomerization process of 20 mM $[Ni(P^{Cy}_2N^{Bn}_2H)_2]^{2+}$ at 25 °C in CD_3CN in the presence of 200 mM aniline with various mixing times. (A) Mixing time = 4 ms. The exchange between the **e**/**x** isomer and the **NiH** intermediate is highlighted in red. (B) Mixing time = 60 ms. The exchange between the **e**/**e** isomer and the **NiH** intermediate is highlighted in blue, and the exchange between the inequivalent ^{31}P nuclei of the **e**/**x** isomer is highlighted in green. (C) Mixing time = 100 ms. The exchange between the **e**/**e** and the **e**/**x** isomers is highlighted in orange.

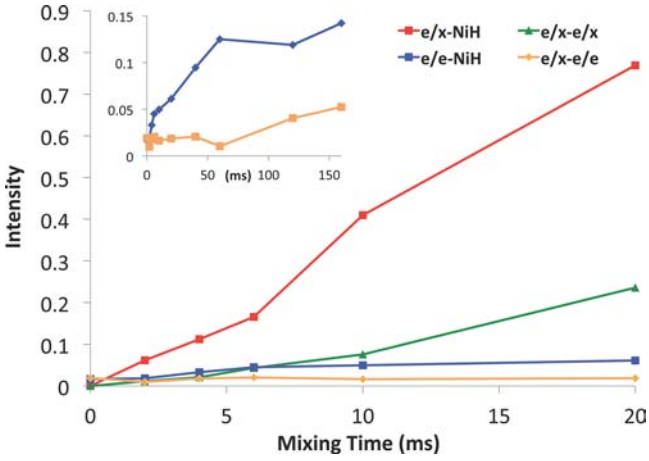

Figure 6. Plot of the ^{31}P EXSY crosspeak intensities as a function of the mixing time. A nonzero initial slope indicates a direct exchange. The inset magnifies the vertical axis of the **e**/**e** ⇆ **NiH** and **e**/**x** ⇆ **e**/**e** exchange for clarity.

possible due to the significant overlap of resonances of the aniline and several resonances of the complexes.

The second-order rate constants k_1, k_{-1}, k_2, and k_{-2} have been determined from the ^{31}P EXSY experiments and are shown in Table 1.[19] The free energy of activation was determined from these values, calculated at 298 K, and are also shown in Table 1 along with the corresponding computationally derived parameters discussed in the following section. The proposed rate equations are shown below, where **B** and $\mathbf{BH}^+$ stand for the base and its conjugate acid, respectively.

$$d[\mathbf{e}/\mathbf{e}]/dt = -k_1[\mathbf{e}/\mathbf{e}][\mathbf{B}]$$

$$d[\mathbf{NiH}]/dt = -k_{-1}[\mathbf{NiH}][\mathbf{BH}^+]$$

$$d[\mathbf{e}/\mathbf{x}]/dt = -k_2[\mathbf{e}/\mathbf{x}][\mathbf{B}]$$

$$d[\mathbf{NiH}]/dt = -k_{-2}[\mathbf{NiH}][\mathbf{BH}^+]$$

To confirm the proposed rate expressions, the order with respect to the base was investigated by monitoring the rate of equilibration as the concentration of aniline was varied. A linear relationship between the concentration of aniline and the rate of formation of 50% of the equilibrium concentration of the **x**/**x** isomer is observed (Supporting Information, Figure S7), consistent with a first-order dependence on aniline.

The slow step of isomerization for both the **e**/**e** and **e**/**x** isomers (pK_a = 13.4 and 13.5, respectively in acetonitrile)[20] is the deprotonation of the doubly protonated Ni(0) complex to form the **NiH** intermediate (k_1 and k_2), dominated by the difference in pK_a between the Ni complex and anilinium (pK_a = 10.6, ΔpK_a = 2.8−2.9). However, deprotonation of the **e**/**x** isomer to form the **NiH** intermediate is 7.5 times faster than deprotonation of the **e**/**e** isomer, despite their similar pK_a values,[20] consistent with easier access for the external base to the exo positioned protons. The reverse reaction, protonation of the hydride, is also favored in the exo position, occurring 24 times faster than protonation at the endo site.

Computational Study of the Mechanism of Isomerization. On the basis of the NMR spectroscopic data, a proposed mechanism involving intermolecular proton transfer accounting for isomerization of the **e**/**e** ⇆ **e**/**x** isomers is

dx.doi.org/10.1021/ja307413x | J. Am. Chem. Soc. 2012, 134, 19409−19424

Scheme 2. Proposed Mechanism of the e/e ⇆ e/x Isomerization Catalyzed by Base (B), Occurring through the NiH Intermediate

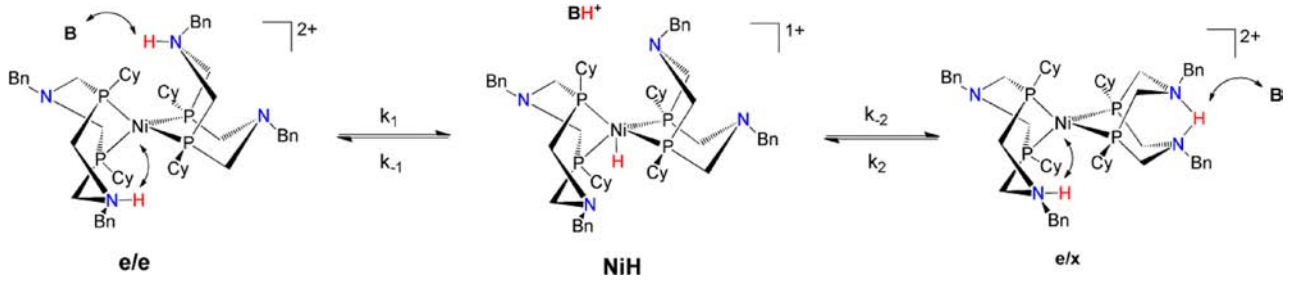

Table 1. Experimental Second-order Rate Constants (k) and Experimental and Theoretical Free Energies of Activation. Activation Free Energies Were Calculated at 298 K According to Pseudo-First Order Kinetics for 20 mM $[Ni(P^{Cy}_2N^{Bn}_2H)_2]^{2+}$ with 10 equiv of Aniline in CH_3CN, or $[Ni(P^{Cy}_2N^{Me}_2H)_2]^{2+}$ in the Case of Theoretical Modeling (k' = k[aniline]) using Transition State Theory[a]

		$\Delta G^{\ddagger}$ (kcal/mol)	
	k (M^{-1} s^{-1})	exp.	theory
e/e → NiH, k_1	7.3 ± 3.6	17.2 ± 0.5	21.4
NiH→ e/e, k_{-1}	2200 ± 500	13.9 ± 0.2	16.9
e/x → NiH, k_2	55 ± 10	16.1 ± 0.1	21.0
NiH→ e/x, k_{-2}	52 000 ± 22 000	12.0 ± 0.3	15.1
e/x → x			26.9
x → e/x			16.2
x/x → x			22.0
x → x/x			11.7

[a] **x** is the monoprotonated exo species defined in Figure 8.

shown in Scheme 2, where **NiH** is observed as the key intermediate between the two isomers. A similar intermediate in the exchange of the **e/x** and the **x/x** isomers was not observed in the NMR spectroscopy studies, which suggests that this slow exchange occurs through one or more high energy intermediates that are short-lived on the NMR spectroscopy time scale.

A comprehensive computational investigation has been carried out to obtain a detailed understanding of the mechanism of isomerization for both the **e/e** ⇆ **e/x** and **e/x** ⇆ **x/x** isomerizations. This detailed understanding will be used to provide a level of mechanistic detail that cannot be obtained from experimental studies, and can be used in the design of improved catalysts for H_2 oxidation and production. All of our calculations were carried out on $[Ni(P^{Cy}_2N^{Me}_2)_2H_n]^{n+}$ (n = 1 or 2) complexes, where the benzyl substituents of the N atoms are replaced by methyl groups to reduce the computational cost. This choice is validated by previous theoretical and experimental investigations[6,12c] and is further discussed below. All of the observed and expected species involved in the isomerization process have been analyzed, including the doubly protonated Ni^0 species (**e/e**, **e/x**, and **x/x** isomers), the proton-hydride species (**e/NiH**), the singly endo protonated species (**e** and **e'**), the singly exo protonated species (**x** and **x'**), and the **NiH** intermediate. These species are illustrated in Figures 1 and 7.

The stepwise mechanism for isomer interconversion between the **e/e** ⇆ **e/x** isomers and the **e/x** ⇆ **x/x** isomers is shown in detail in Figures 8 and 9, respectively. Isomerization requires the initial formation of a hydrogen-bonded complex (referred

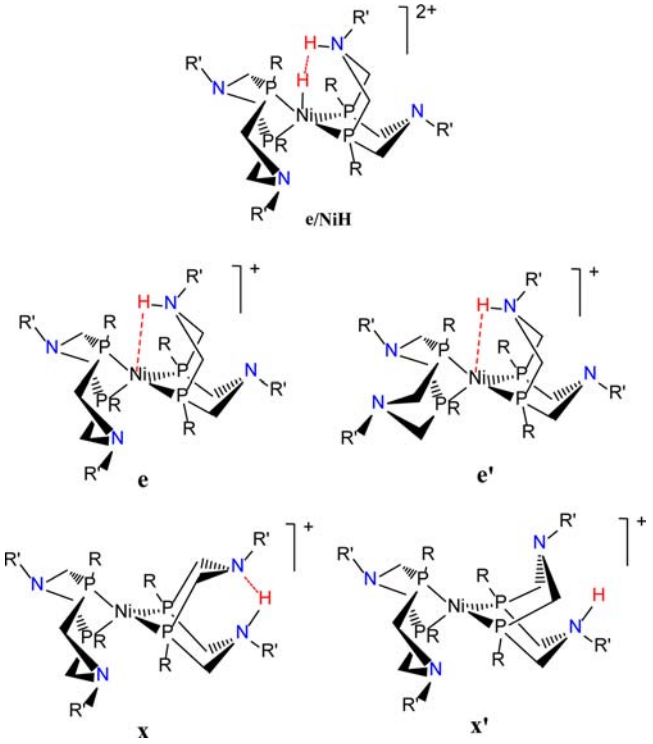

Figure 7. Intermediates considered in the theoretical modeling.

to as the association complex) between $[Ni(P^{Cy}_2N^{Me}_2H)_2]^{2+}$ and the base (steps 1 and 7 in Figure 8 and steps 1′ and 5′ in Figure 9). This reaction is then followed by a sequence of steps, whose order depends on the starting isomer (**e/e**, **e/x**, or **x/x**) and deprotonation site (endo or exo). These steps include the conformational change of one of the six-membered rings of the ligand, such as boat-chair conversions (e.g., step 6, Figure 8), *inter*molecular proton transfers (e.g., steps 3 and 5, Figure 8) and *intra*molecular proton transfers mediated by the metal center (e.g., steps 2 and 4, Figure 8). Each step for the **e/e** ⇆ **e/x** and the **e/x** ⇆ **x/x** isomerization is presented individually in the following section. It should be noted that Figures 8 and 9 show only the lowest energy pathways that were found. Alternative (higher free energy) pathways are provided in the Supporting Information.

Aniline Binding/Dissociation (steps 1, 7, 1′, 5′). To investigate the binding of aniline, we performed hybrid density functional theory/molecular mechanics metadynamics simulations[12b] on the formation of the association complexes **B:e/x** and **e/x:B** with the aniline approaching the endo position and the exo position (step 1′ and step 7, respectively) in acetonitrile. The structural and energetic analysis presented

dx.doi.org/10.1021/ja307413x | J. Am. Chem. Soc. 2012, 134, 19409−19424

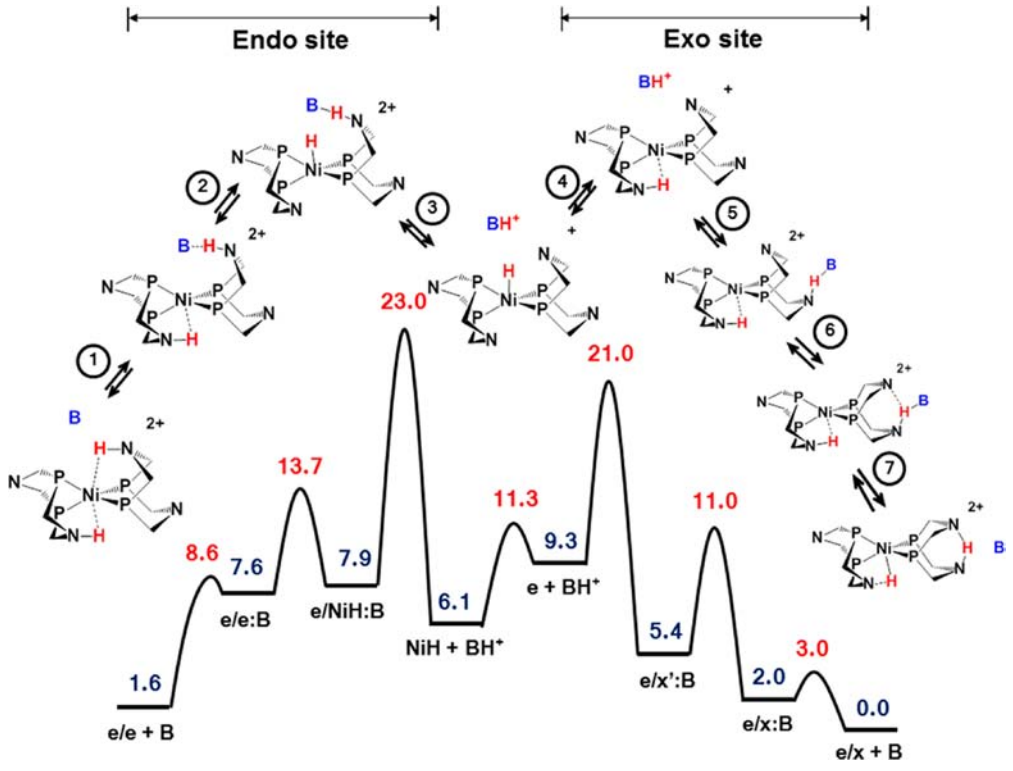

Figure 8. Free energy diagram for the **e**/**e** ⇆ **e**/**x** isomerization mechanism catalyzed by aniline, **B**, in acetonitrile. The relative free energies with respect to **e**/**x** + **B** (in kcal/mol) of the various intermediates and the transition states are indicated with blue and red numbers, respectively. The free energies of bimolecular steps as well as of the boat-to-chair inversion (step 6) were calculated from hybrid QM/MM metadynamics simulations; all of the other free energies were obtained from QM calculations with a polarizable continuum description of the solvent. The R and R' groups are not shown for clarity.

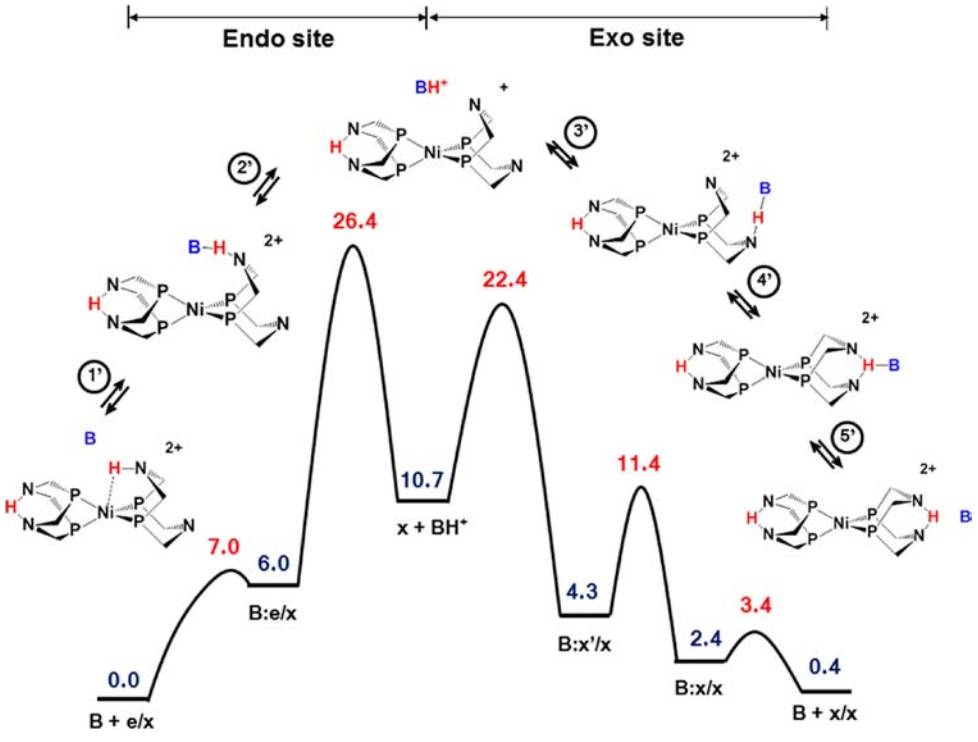

Figure 9. Free energy diagram for the **e**/**x** ⇆ **x**/**x** isomerization mechanism catalyzed by aniline, **B**, in acetonitrile. The relative free energies with respect to **e**/**x** + **B** (in kcal/mol) of the various intermediates and the transition states are indicated with blue and red numbers, respectively. The free energies of bimolecular steps as well as of the boat-to-chair inversion (step 4') were calculated from hybrid QM/MM metadynamics simulations; all of the other free energies were obtained from QM calculations with a polarizable continuum description of the solvent. The R and R' groups are not shown for clarity.

dx.doi.org/10.1021/ja307413x | J. Am. Chem. Soc. 2012, 134, 19409−19424

below for the **e**/**e**, **e**/**x** and **x**/**x** isomers suggests that the binding of aniline to each side of the **e**/**x** isomer is also representative of the binding of aniline to the **e**/**e** and **x**/**x** isomers; therefore the binding free energies and binding activation barriers were not calculated for **e**/**e** and **x**/**x** isomers.

The free energy landscape for aniline binding to the endo position of the **e**/**x** isomer is shown in Figure 10. The

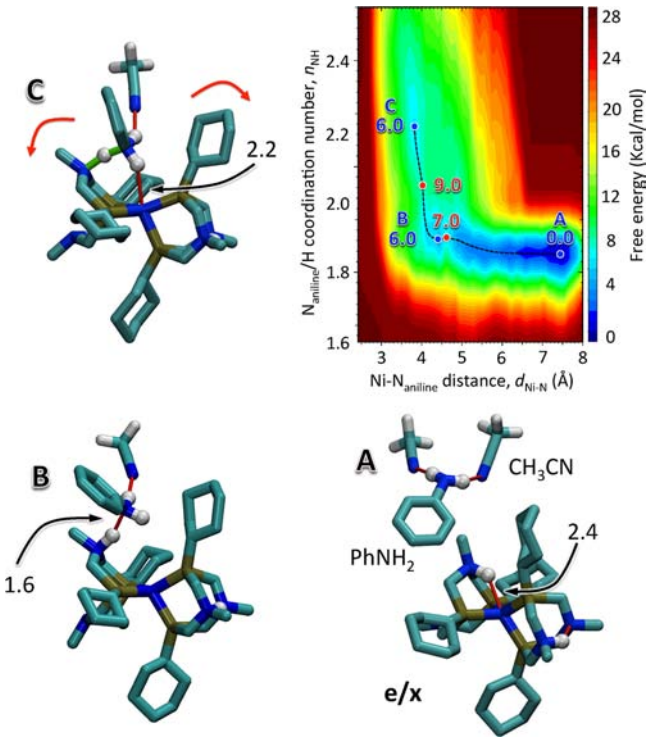

Figure 10. Upper right panel: Free energy landscape for the binding of aniline to the endo position of the **e**/**x** isomer as a function of the distance (d_{Ni-N}) between the Ni center and the N atom of aniline, and as a function of the fractional number (n_{NH}) of hydrogen atoms surrounding the N atom of aniline (coordination number, see Materials and Methods, Computational Details). Local minima and transition states between them are marked with blue and red dots, respectively. Free energies at minima and transition states are also reported using the same colors. The dotted lines indicate the lowest free energy pathway. Representative configurations of the minima on the free energy surface are shown in panels A, B, and C. Hydrogen bond interactions are shown as red lines; in C the green sticks indicate that the H atom is shared between the two N atoms (see text). The red arrows in C indicate the overall movement of the pendant amine and the proximal cyclohexyl group upon binding of the base. In all of the figures, acetonitrile molecules hydrogen bonded to aniline are also shown. In A, B and C, selected average distances (in Å) are also reported. For clarity, nonprotic H atoms on the Ni complex and aniline are not shown.

formation of the **B**:**e**/**x** association complex requires the initial crossing of an activation barrier (7.0 kcal/mol). Upon binding, aniline partially desolvates (Figure 10A and B). As discussed below, desolvation is an important part of the overall reaction free energy. Once aniline enters the coordination sphere of the metal center (d_{Ni-N} < 4.5 Å), the pendant amine N−H···Ni hydrogen bond is broken and the protonated pendant amine N−H reorients to hydrogen bond with aniline (Figure 10B). A further decrease of the Ni/aniline distance causes the formation of a hydrogen bond between the N−H bond of the aniline and the metal center (activation barrier of 3 kcal/mol, Figure 10C). The interaction between aniline and the pendant amine is very strong through the asymmetrically shared proton, with the pendant amine/proton distance slightly shorter than the aniline/proton distance (1.2 Å and 1.4 Å, respectively). The two bound situations (Figure 10B and Figure 10C) are isoenergetic, with state C kinetically more stable against the dissociation of aniline than state B (the activation barrier for the dissociation of aniline is ∼3.0 kcal/mol and ∼1.0 kcal/mol, respectively). In summary, the formation of the **B**:**e**/**x** association complex is endothermic by 6 kcal/mol.

In contrast, the formation of the **e**/**x**:**B** association complex (Figure 8, step 7) is endothermic by only 2.0 kcal/mol with a small activation barrier (3.0 kcal/mol, Figure 8 and 11). The hydrogen bonding between aniline and the pendant amine is weak, consistent with the long NH···N distance of about 2.9 Å (Figure 11B). The pinched hydrogen bond in the **e**/**x** complex is perturbed very little by the association of aniline. The association complex of Figure 11B evolves easily to a second complex slightly higher in free energy (Figure 11C), where the pinched structure is distorted ($d_{N\cdots H}$ = 2.7 Å) and a new, cyclic hydrogen bond arrangement is formed where aniline receives a hydrogen bond from the protonated pendant amine ($d_{N(base)\cdots H}$ = 1.8 Å) and donates a hydrogen bond to the nonprotonated pendant amine ($d_{H(base)\cdots N}$ = 3.5 Å, Figure 11C).

Intermolecular Proton Transfer and Dissociation of Anilinium. For either endo or exo protonated isomers, the metadynamics simulations revealed that proton transfer from the metal complex to the aniline to form anilinium, and the dissociation of anilinium from the complex, is a continuous process with no stable intermediate (i.e., anilinium bound to the singly protonated Ni complex). Similarly, the reverse process is also concerted, in that the association complex is not stable against proton transfer from the anilinium back to the metal complex. This is illustrated in Figure 12, which shows the calculated free energy landscape for deprotonation from the exo position. The results are summarized in Table 2, along with results for deprotonation from both endo and exo positions for various additional isomers (free energy landscapes for these additional isomers are included in the Supporting Information).

Although the overall process for proton transfer to aniline and the dissociation of anilinium is concerted, the activation free energy for this process, $\Delta G^{\ddagger}_{d}$, can be decomposed into two parts (Figure 12): proton transfer to aniline ($\Delta G^{\ddagger}_{d,H+}$) and subsequent dissociation of anilinium ($\Delta G^{\ddagger}_{d,diss}$). The largest contribution to this overall barrier is the dissociation of anilinium from the metal complex.

e/e ⇆ e/x Isomerization: Deprotonation at the Endo Site (steps 2 and 3). For the **B**:**e**/**e** association complex, the transfer of a proton to aniline and the dissociation of the resulting anilinium can either precede or follow the transfer of a proton from the endo position to the metal center to generate a metal hydride. Both pathways were considered, and the lower energy pathway was found to start with the transfer of the endo proton to the metal center to generate, after a facile rotation around the metal center,[12c] the metal-hydride in **e**/**NiH**, as shown in steps 2 and 3 of Figure 8.

e/e ⇆ e/x Isomerization: Deprotonation at the Exo Site (steps 4, 5 and 6). Deprotonation on the exo side requires the chair to boat conformational change of one of the two six-membered rings pinching the exo proton (step 6). Our calculations indicate that this conformational change preferentially occurs after the formation of the **e**/**x**:**B** association complex, but before the transfer of the proton. The barrier for

dx.doi.org/10.1021/ja307413x | J. Am. Chem. Soc. 2012, 134, 19409−19424

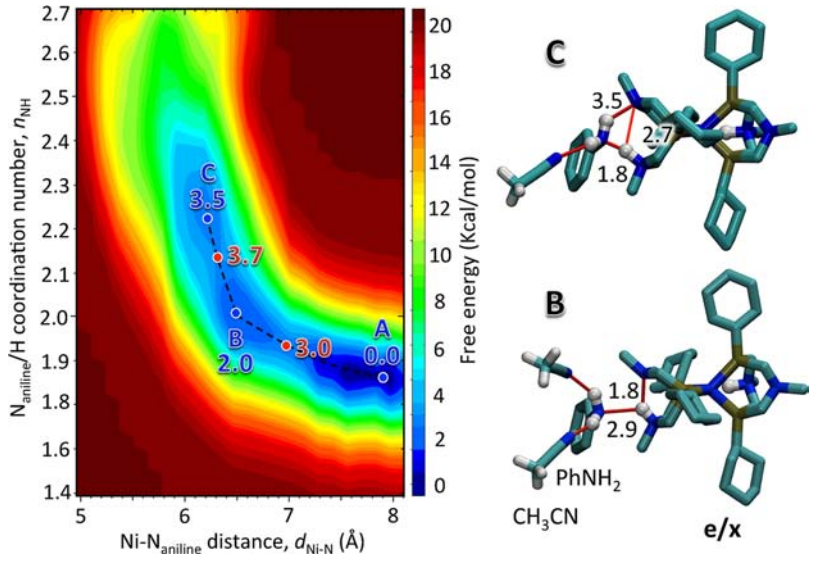

Figure 11. Left panel: Free energy landscape for the binding of aniline to the exo position of the **e**/**x** isomer. Right panel: representative configurations of the two bound minima on the free energy surface. The minimum A represents the dissociated state and is not illustrated. See caption of Figure 10 for further details.

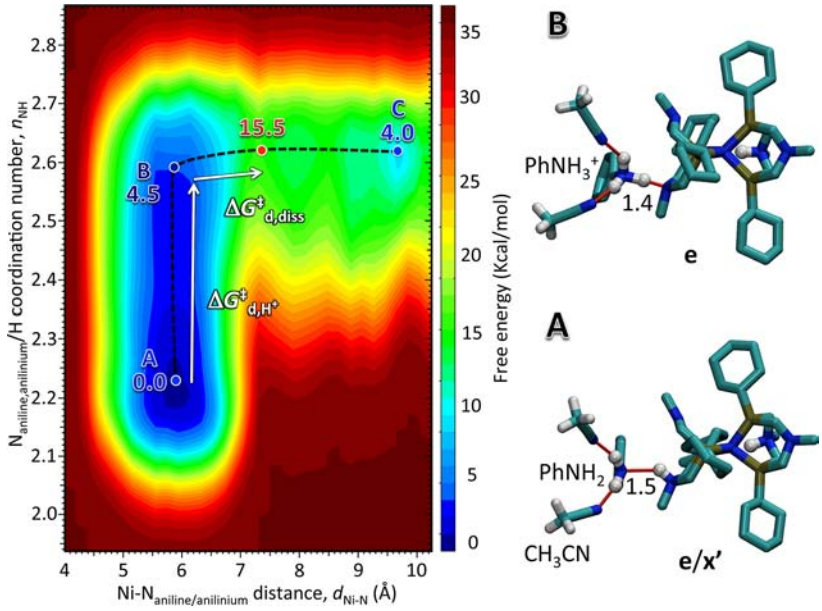

Figure 12. (Left) free energy landscape for the concerted intermolecular proton transfer to aniline in the association complex and subsequent dissociation of anilinium from the exo site of the **e**/**x** isomer. (Right) Representative configurations of the association complex with aniline (A) and anilinium (B). Note that B is not a minimum on the free energy surface. The minimum C represents the unbound **e** + anilinium state (Figure 9, step 4, not illustrated). The white arrows define the two contributions to the activation barrier: proton transfer to aniline ($\Delta G^{\ddagger}_{d,H^+}$) and subsequent dissociation of anilinium ($\Delta G^{\ddagger}_{d,diss}$). See caption to Figure 10 for further details.

the inversion of one of the exo rings is 15.1 kcal/mol for **e**/**x** (Supporting Information, Figure S11) and 10.4 kcal/mol for **e**/**x:B** (Figure 10). During the conformational change, the intramolecular hydrogen bond between the pinched rings is replaced by the intermolecular hydrogen bond with the aniline, thus reducing the energy penalty to isomerize the other ring.

The intermolecular proton transfer to aniline and the subsequent dissociation of anilinium (step 5) occurs preferentially from the nonpinched form of **e**/**x**′**:B** (i.e., after the conformational change), where **e**/**x**′ indicates the exopositioned, nonpinched isomer. The overall activation barrier for dissociation of anilinium from **e**/**x:B** is 12.5 kcal/mol higher than that from **e**/**x**′**:B**, which is a result of two distinct factors. First, proton transfer from the pinched form (**e**/**x:B**) is energetically disfavored relative to the nonpinched form (**e**/**x**′**:B**, Table 2). Second, there are two strong hydrogen bonds between anilinium and the deprotonated form of the pinched **e**/**x** complex that need to be broken (see species **e'**, Supporting Information, Figure S12 and Table 2), whereas only one hydrogen bond has to be cleaved in the dissociation of anilinium from **e**/**x**′**:B**.

e/x ⇆ x/x Isomerization. The mechanism for the **e**/**x** ⇆ **x**/**x** isomerization (Figure 10) shares many similarities with the **e**/**e** ⇆ **e**/**x** isomerization, as both involve deprotonation from the endo position. However, the **e**/**x** ⇆ **x**/**x** isomerization requires the crossing of larger activation barriers than for the

dx.doi.org/10.1021/ja307413x | J. Am. Chem. Soc. 2012, 134, 19409−19424

Table 2. Activation Free Energy $\Delta G^{\ddagger}_{d}$ (in kcal/mol) for the Transfer of a Proton to Aniline and Dissociation of Anilinium from Different Species[a]

reactant	product	$\Delta G^{\ddagger}_{d}$	$\Delta G^{\ddagger}_{d,H+}$	$\Delta G^{\ddagger}_{d,diss}$
B:e/NiH	**NiH** + BH^+	15.0	6.0	9.0
B:e/e	**NiH** + BH^+	17.0	7.0	10.0
e/x:B	**e′** + BH^+	(28.0)	8.0	(20.0)
e/x′:B	**e** + **B**	15.5	4.5	11.0
B:e/x	**x** + BH^+	20.4	7.0	13.4
B:x′/x	**x** + BH^+	18.1	4.5	13.6

[a]Individual contributions due to the proton transfer ($\Delta G^{\ddagger}_{d,H+}$) and to the dissociation of anilinium ($\Delta G^{\ddagger}_{d,diss}$) are also reported.

e/e ⇆ **e/x** isomerization. The primary source of this difference is in the formation of the **x** species rather than the **NiH** intermediate, as the latter was determined to be 4.6 kcal/mol more stable.

Overall Activation Barriers for Isomerization. The effective activation barriers obtained from the EXSY experiments and the overall activation free energies yielded by the isomerization mechanisms presented above are compared in Table 1. While the complexes studied experimentally ($[Ni(P^{Cy}_2N^{Bn}_2H)_2]^{2+}$) and theoretically ($[Ni(P^{Cy}_2N^{Me}_2H)_2]^{2+}$) are not identical, the agreement in the results from each approach with these similar complexes is satisfactory. The proposed mechanisms (Figures 8 and 9) explain why the **e/x** ⇆ **x/x** isomerization is slower than the **e/e** ⇆ **e/x** isomerization, as discussed in the previous paragraph. Additionally, the proposed mechanisms and barriers are in agreement with the experimental results that the **e/x** ⇆ **NiH** exchange process is faster than the **e/e** ⇆ **NiH** exchange. The overall theoretical deprotonation barriers to form the **NiH** intermediate are about 4.5 kcal/mol higher than the experimental barriers, which is primarily due to the difference in the pK_a of the pendant amine between $[Ni(P^{Cy}_2N^{Bn}_2H)_2]^{2+}$ (experimentally determined pK_a = 13.4) and $[Ni(P^{Cy}_2N^{Me}_2H)_2]^{2+}$ (calculated pK_a = 15.3).[21,22]

Aniline/Anilinium Association and Dissociation. The largest contributions to the overall barrier for the isomerization processes are the association of aniline to the endo position and, to a greater extent, the association and dissociation of anilinium at both endo and exo positions. In the previous paragraphs, the barrier for the dissociation of anilinium was presented in terms of the energy cost associated with the breaking of the hydrogen bonding interaction between anilinium and the Ni complex. To quantify this energy cost and elucidate the origin of the barrier for the association reaction both of aniline and anilinium, the overall binding energy (ΔE_{bind}) between the aniline or anilinium and the corresponding Ni complex has been separated into two components. These components are calculated as a function of the relative distance, *r*, and include both the energy necessary to distort the nickel complex (steric penalty) in order to accommodate aniline or anilinium (ΔE_{dis}) and the interaction energy between the two species in acetonitrile solution ($\Delta E_{int\text{-}sol}$, mostly due to the hydrogen bonding and the electrostatic interaction). The two contributions have been calculated at the QM level with a continuum description of the solvent as discussed in the Computational Details in the Experimental section, where the validity of this decomposition is also discussed. For a more detailed theoretical analysis of the various contributions to the steric hindrance and their effect on chemical reactivity, we would like to refer the reader to the work by Bickelhaupt and co-workers.[23]

The results of the energy decomposition are shown in Figure 13. There is a steric penalty for the binding of aniline to the

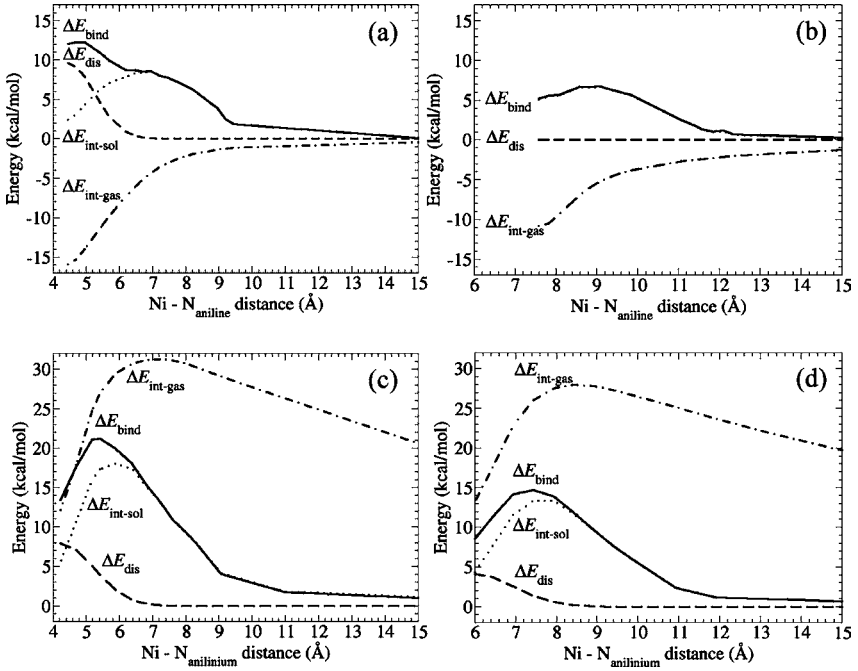

Figure 13. Binding energy decomposition as a function of the relative distance between the Ni complex and the base (aniline) or acid (anilinium). The total binding energy (ΔE_{bind}, solid line) is broken down into two components: distortion energy (ΔE_{dis}, dashed line) and solvation energy ($\Delta E_{int\text{-}sol}$, dotted line). The gas-phase interaction energy ($\Delta E_{int\text{-}gas}$, dotted-dashed line) is also reported for comparison. This decomposition is illustrated for four cases: binding of aniline to (a) the endo and (b) the exo position of the **e/x** isomer; binding of anilinium to (c) the endo position of the **NiH** intermediate and (d) the exo position of the **e** intermediate.

dx.doi.org/10.1021/ja307413x | J. Am. Chem. Soc. 2012, 134, 19409−19424

Scheme 3. Mechanism of Hydrogen Oxidation/Production[a]

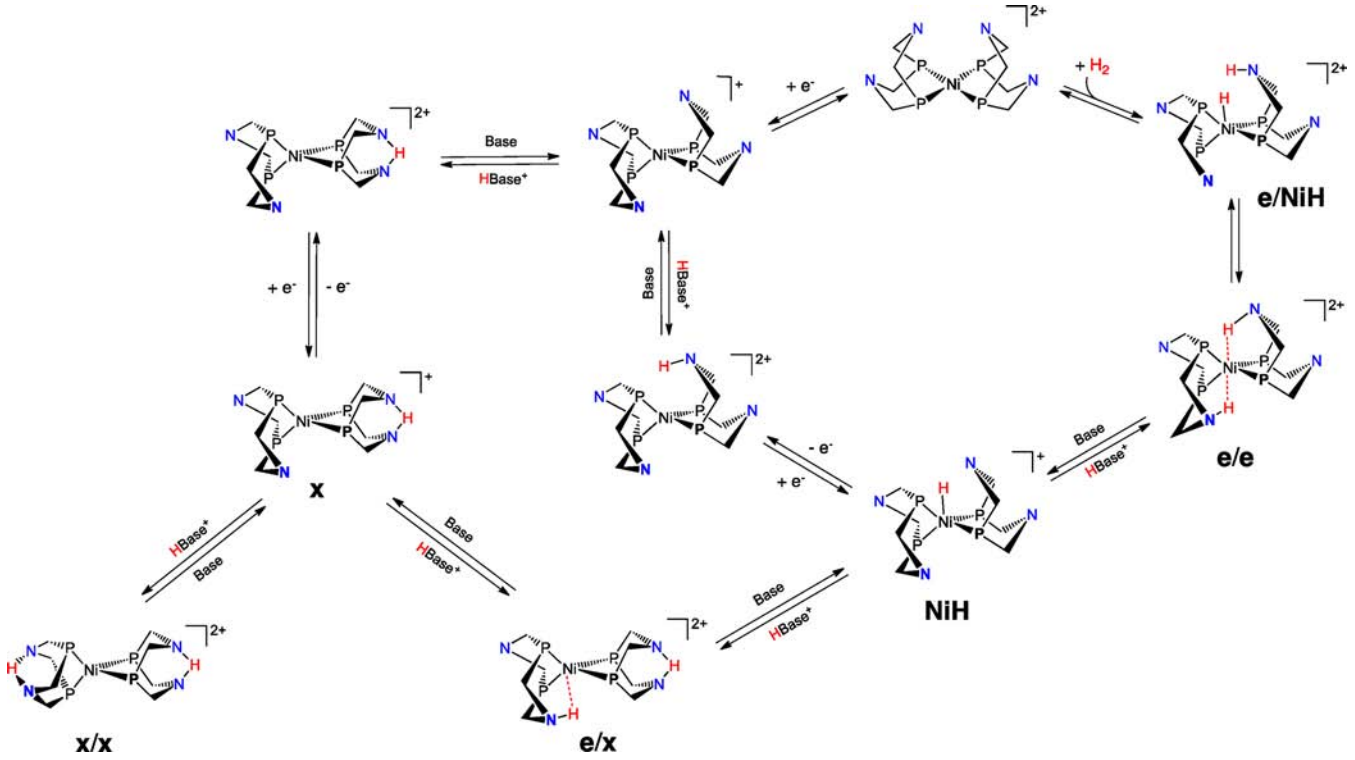

[a]Protonation of exo (pinched) positions results in branching to less productive pathways. The R and R' groups are not shown for clarity.

endo position as compared to the exo position (compare for instance Figure 13a to b). In order to accommodate the aniline or anilinium in the endo position, the pendant amine on one ligand and the cyclohexyl group on the opposite ligand have to move away from each other, as illustrated by comparing Figure 10A and C. The ΔE_{dis} term for binding to the endo position is 9.2 and 9.6 kcal/mol for the **e**/**e** and **e**/**x** isomers, respectively. In contrast, the ΔE_{dis} for the binding to the exo position is only about 0.1 kcal/mol for both the **e**/**x** and **x**/**x** isomers. For the **NiH** intermediate, the energy cost is slightly smaller for the structural distortion required to form the association complex with anilinium in the endo position (ΔE_{dis} = 7.3 kcal/mol) than for the association complex between aniline and the endo position of the **e**/**e** and **e**/**x** isomers.

As shown in Figure 13, the interaction energy $\Delta E_{int\text{-}sol}$ was found to be significantly different for the binding of aniline to the doubly protonated species compared to the binding of anilinium to the singly protonated species. For the latter case, the electrostatic repulsion between the two monocations is partially compensated for by the dielectric screening of the solvent, however, as the distance decreases, the binding of the charged anilinium is increasingly unfavorable compared to that of the neutral aniline. While the electrostatic repulsion decreases the stability of anilinium binding relative to aniline, the increase in the strength of the hydrogen bonds for anilinium compared to aniline makes up for this electrostatic effect. In the case of aniline, desolvation largely contributes to the binding activation barrier. This is evident from the comparison of $\Delta E_{int\text{-}sol}$ with corresponding quantity $\Delta E_{int\text{-}gas}$ calculated in absence of solvent, which is also reported in Figure 13.

DISCUSSION

The electrocatalytic interconversion of H_2 to protons and electrons by $[Ni(P^R_2N^{R'}_2)_2]^{2+}$ complexes requires the delivery or removal of protons to/from the pendant amine, specifically at the endo positions with respect to the metal. Only protons endo to the metal center are properly positioned for catalysis (Scheme 1). In $[Ni(P^R_2N^{R'}_2)_2]^{2+}$ systems, protons can be positioned either endo or exo. The isomers with exo positioned protons are not catalytically competent and therefore the interconversion of the exo protons to the endo position is necessary for catalytic turnover to occur. The experimental and theoretical work reported here shows that the precise delivery of protons and the rate of protonation/deprotonation are regulated in a nontrivial way by the combination of three factors: steric effects, hydrogen bonding, and electrostatic interactions. These concepts and their relevance to the design of more efficient catalysts for H_2 oxidation and production are further elaborated in the following discussion.

Kinetic Products of Protonation. Access to the endo site is hindered, as indicated by the kinetic preference to protonate at the exo site in the $[Ni^0(P^{Cy}_2N^{Bn}_2)_2]$ complex (Figures 2 and Supporting Information S3) and explained by theoretical modeling (Figures 8 and 10). Protonation of this zerovalent nickel complex provides insight into the first steps of the catalytic cycle for hydrogen production, in that the initial product of protonation is almost exclusively the catalytically unproductive **x**/**x** isomer (see Scheme 1 and Figure 1). Exo protonation is also observed when acid is added to the **NiH** intermediate, as the unproductive **e**/**x** isomer is the major product; the **e**/**e** isomer is not observed. Consistent with the current NMR results and previous electrochemistry experiments,[5a] the present theoretical modeling indicates that steric

dx.doi.org/10.1021/ja307413x | J. Am. Chem. Soc. 2012, 134, 19409−19424

hindrance is the major discriminator promoting protonation at the exo site rather than the endo site.

Mechanism of Isomer Interconversion. Based on the observation that exo protonation is kinetically favored, isomerization to the catalytically active **e**/**e** isomer may be an essential process for the majority of the catalyst. From the NMR exchange spectroscopy (^{31}P EXSY) experiments, the **e**/**e** and **e**/**x** isomers can interconvert quickly, and the rates of interconversion are dependent upon conditions but are similar to catalytic rates for hydrogen production. In contrast, for the $[Ni(P^{Cy}_2N^{Bn}_2H)_2]^{2+}$ complex, the interconversion of the **x**/**x** isomer to the **e**/**e** and **e**/**x** isomers is significantly slower, taking minutes to hours to interconvert. The proposed mechanism of isomer interconversion in the presence of a base such as aniline (**e**/**e** ⇆ **e**/**x** in Figure 8 and **e**/**x** ⇆ **x**/**x** in Figure 9) involve several similar steps. The mechanism is consistent with the EXSY results for $[Ni(P^{Cy}_2N^{Bn}_2H)_2]^{2+}$ (Figure 5), which establishes that deprotonation of the **e**/**x** isomer at the exo site to form the **NiH** intermediate is followed by protonation of **NiH** at the endo site to form the **e**/**e** isomer. From the theoretical studies, the reaction pathway connecting the isomers is uphill to generate the **NiH** intermediate for the **e**/**e** ⇆ **e**/**x** isomerization or to generate the exo mono proton species **x** for the **e**/**x** ⇆ **x**/**x** isomerization (Figures 8 and 9, respectively). Each step contributes to the overall free energy barrier. However, the dissociation of anilinium or its reassociation during the reprotonation stage constitutes the largest contributions to the activation barrier of these processes. These contributions are primarily due to strong hydrogen bonding interactions for the dissociation and electrostatic repulsion between anilinium and the monocationic species **NiH** or **e** for the reprotonation reaction. In addition, because of steric hindrance, the association of both aniline and anilinium to the endo position is further disfavored with respect to the more accessible exo position.

In the presence of 10 equivalents of aniline, the interconversion of the **e**/**x** isomer and the **NiH** intermediate is faster in both directions than the interconversion of the **e**/**e** isomer and the **NiH** intermediate, as measured by ^{31}P EXSY, even though the pK_a values are about the same for the **e**/**e** and **e**/**x** isomers.[20] The difference in steric accessibility of the endo and exo sites is the principal cause of the different reactivity (as presented in the Results section and summarized in Table 1 and Scheme 2). Computational results show that the major contribution to this difference is the large distortion energy required to form the association complex at the endo site as compared to the exo site.

Implications for Hydrogen Production Catalysis. The kinetically preferred protonation site is exo with respect to the metal, and the resulting **x**/**x** species undergoes slow isomerization to the **e**/**e** and **e**/**x** isomers. Although the results of the current work are based on H_2 oxidation catalysts, the extension of these results to H_2 production catalysts suggests that a large fraction of the catalyst exists as the **x**/**x** isomer, which requires isomerization to the **e**/**e** isomer prior to H_2 elimination (Scheme 3). For $[Ni(P^{Cy}_2N^{Bn}_2H)_2]^{2+}$, the isomerization of the **x**/**x** isomer to the **e**/**x** isomer and subsequently to the **e**/**e** isomer may considerably reduce the catalytic efficiency because it requires the formation of the **x** intermediate, which is substantially higher in energy based on both the theoretical modeling (Figure 9) and the lack of observation of the **x** species in the spectroscopic studies. Following the generation of the **x** species, formation of the **e**/**x** isomer requires the protonation of the **x** species at the endo site (Figure 9, step 3′), which is kinetically disfavored, as described above.

If **x**/**x** to **e**/**e** isomerization were limiting hydrogen production catalysis, the kinetics of catalysis would be dominated by the largest barriers along this pathway, which are dependent on both the ability of the acid to protonate endo and on the ability of the conjugate base to deprotonate from the exo position. Although these barriers will be influenced by the specific substituents on the ligands, an accumulation of the exo protonated isomers under catalytic conditions is expected. The build-up of the **x**/**x** isomer has been recently observed in the protonation of the hydrogen production catalyst, $[Ni^0(P^{Ph}_2N^{Bn}_2)_2]$, at low temperature.[24] Protonation of the $[Ni^0(P^{Ph}_2N^{Bn}_2)_2]$ complex resulted in the formation of the **x**/**x** isomer, which slowly disappeared as H_2 was produced, over approximately 4 h. No other doubly protonated intermediates were observed prior to H_2 elimination, suggesting that the conversion of the **x**/**x** isomer to the **e**/**x** isomer is slower than the subsequent isomerization to **e**/**e**, which precedes H_2 elimination. These previous results are consistent with the current results in which the interconversion between the **e**/**x** and **e**/**e** isomers is much faster than the interconversion between the **e**/**x** and **x**/**x** isomers. While the pendant amines incorporated in H_2 production catalysts are typically less basic than in the complexes studied herein, exo protonation and the subsequent isomerization may represent a significant restriction in the catalytic rates that can be achieved for this family of catalysts.

Further evidence that exo protonation and slow isomerization decreases the rate of H_2 production comes from the different maximum rates observed with different acids for a single catalyst.[5a,6,25] For example, different maximum turnover frequencies (TOFs) are observed when $[(DMF)H]^+$ vs $[(2,6\text{-}DCA)H]^+$ are used, even though acid independence is reached in both cases.[5a] If the rate of protonation alone were the rate-determining step in catalysis, it would be expected that the same maximum turnover frequency would be achieved with any acid, but may require differing concentrations. The dependence of the mechanism of isomerization on both protonation and deprotonation proposed here helps to explain why this is not observed.

Finally, according to our theoretical modeling, the dissociation of the hydrogen-bonded complex (the catalyst and the conjugated acid of the external base) is the step with the highest free energy barrier, regardless of the deprotonation site (endo vs exo). This suggests that the formation of strong hydrogen bonds in the association complex is another factor limiting the efficiency of this class of catalysts. This result suggests a new possibility for enhancing the catalytic efficiency by changing the hydrogen bonding interactions to lower the barrier for dissociation, and therefore increase the rates of protonation/deprotonation.

Implications for Hydrogen Oxidation Catalysis. For hydrogen oxidation, endo deprotonation is a critical step in the catalytic cycle (Scheme 1). The **e**/**e** isomer is the kinetic product of H_2 addition for $[Ni(P^{Cy}_2N^{Bn}_2)_2]^{2+}$ and other $[Ni(P^{Cy}_2N^{R'}_2)_2]^{2+}$ complexes,[6,11] and here we have shown the deprotonation from the endo position is a high energy process. The present study shows that, using aniline, the barrier for deprotonation at the endo site is 17.2 kcal/mol for $[Ni(P^{Cy}_2N^{Bn}_2)_2]^{2+}$ based on the NMR spectroscopy experiments and 21.4 kcal/mol for $[Ni(P^{Cy}_2N^{Me}_2)_2]^{2+}$ from theoretical

modeling (Table 2 and Figure 8). These barriers are similar to the overall barrier (around 15 - 16 kcal/mol) for H_2 oxidation as determined from the measured TOF's for $[Ni(P^{Cy}_2N^{tBu}_2)_2]^{2+}$, $[Ni(P^{Cy}_2N^{Bn}_2)_2]^{2+}$, and $[Ni(P^{Cy}_2N^{Me}_2)_2]^{2+}$ using significantly stronger bases.[6,12c,14] Similar to H_2 production catalysis, different maximum TOF's are observed depending on the base used, where rates obtained with *n*-butylamine are faster than those with *t*-butylamine.[10] This supports the proposal that steric accessibility of the endo site may limit the rate of deprotonation, which, in turn, may limit catalytic rates for H_2 oxidation.

Relevance to [FeFe] Hydrogenase and Other Functional Mimics. The need for efficient and specific proton removal and delivery is accomplished in the [FeFe]-hydrogenase enzyme active site by using the protein scaffold to tightly control the structure of the active site while also carefully positioning the single pendant amine. The precise control of the active site structure in enzymes is pertinent to the present results on the synthetic $[Ni(P^R_2N^{R'}_2)_2]^{2+}$ complexes, which form unproductive isomers and have poorly optimized proton delivery to the endo position. Similar to these results, in the bimetallic system reported by Rauchfuss et al.,[26] the product of heterolytic cleavage of H_2 is a protonated amine on the bridging dithiolate ligand and a terminal Fe-hydride species that isomerizes readily to a bridging hydride complex. The formation of this bridging hydride is similar to the generation of the exo protonated $[Ni(P^R_2N^{R'}_2)_2]^{2+}$ complexes, as both have a proton trapped in a "pinched" position. The structure of the active site of the hydrogenase enzyme is controlled to prevent this sort of deactivation. Furthermore, the transfer of protons at the active site of the [FeFe]-hydrogenase enzyme is facilitated through the use of a secondary pendant amine as the proton relay in the second coordination sphere,[1a] rather than the tertiary pendant amines used in the present work. Unlike the tertiary amines, protonation of a secondary pendant amine results in protons in both the endo and exo positions, facilitating proton transfer either to or from the metal. For both the control of geometry (and the corresponding reactivity) and in the delivery of protons using secondary amines, the precise control over the structure and activity found in enzymes provides inspiration and direction for development of future catalysts through the delivery of protons to the endo position.

SUMMARY AND CONCLUSIONS

Proton delivery and removal has been shown to be a possible bottleneck in the electrocatalytic oxidation and production of H_2 using $[Ni(P^R_2N^{R'}_2)_2]^{2+}$ complexes. Proton delivery and removal at the active site in the $[Ni(P^{Cy}_2N^{Bn}_2)_2]^{2+}$ catalyst was found to be limited by the accessibility of the endo position of the pendant amines due to steric hindrance. For H_2 oxidation catalysts, the deprotonation of the endo site may be the rate-determining step, and increasing the steric accessibility of the endo site is expected to increase catalytic rates. For H_2 production, this steric inaccessibility results in a kinetic preference for exo protonation, leading to formation of isomers that are detrimental to catalysis. In the present studies, the rate of isomerization of the kinetically preferred protonation product, **x**/**x**, is substantially slower than the isomerization of **e**/**x** to **e**/**e**, suggesting a possible limitation on catalytic rates for analogous H_2 production catalysts. Directing protonation to the endo site and avoiding the **x**/**x** and **e**/**x** species are critical to achieving the full capability of these $[Ni(P^R_2N^{R'}_2)_2]^{2+}$ catalysts for hydrogen production.

EXPERIMENTAL SECTION

Materials. Solvents were prepared using an Innovative Technologies Pure Solv solvent purification system unless otherwise noted. Dimethylformamide was purchased from Sigma Aldrich as the highest purity available (50 ppm H_2O) and used as received. CD_3CN was dried by distillation from P_2O_5. Aniline was dried with KOH and purified by distillation. Ultra high purity (99.999%) hydrogen was dried by passage through an in-line drier (OxypurgeN) in series with an AT indicating cartridge (Alltech). All other reagents were used as received.

Synthesis of Ni Complexes. Previously reported procedures were followed for the synthesis of $[Ni(P^{Cy}_2N^{Bn}_2)_2][BF_4]_2$, $[Ni^0(P^{Cy}_2N^{Bn}_2)_2]$, and $[HNi(P^{Cy}_2N^{Bn}_2)_2][BF_4]$.[12c] The spectral properties are consistent with those previously reported.[11,12c]

NMR Spectroscopy Sample Preparation. All samples and stock solutions were prepared under a nitrogen atmosphere. A typical sample preparation procedure for EXSY experiments is as follows: 19 mg (15 μmol) $[Ni(P^{Cy}_2N^{Bn}_2)_2]^{2+}$ was dissolved in 0.7 mL CD_3CN to result in a 20 mM solution. The solution was purged with H_2 for ~1 min to quantitatively generate $[Ni(P^{Cy}_2N^{Bn}_2H)_2]^{2+}$, confirmed by a visible color change from purple to pale yellow and $^{31}P\{^1H\}$ NMR spectroscopy. To this solution, 20 μL of a 0.2 M (4 μmol) *tert*-butylimino-tri(pyrrolidino)phosphorane, BTPP, solution was added followed by the addition of 15 μL (165 μmol) aniline. The sample was allowed to equilibrate at 25 °C for at least 15 min before data acquisition. 0.2−0.25 equivalents of the base, BTPP (pK_a = 28.4 for H-BTTP$^+$),[27] were added to samples used for the EXSY kinetic studies in order to increase the concentration of the hydride species. This was necessary to avoid saturation of magnetization during the exchange processes. In the absence of aniline, BTTP and the hydride species alone could not facilitate significant isomerization on the EXSY time scales, (Supporting Information Figure S7).

For isomer equilibration studies, varying molar equivalents of aniline, dimethyl formamide (DMF) or 2,6-dichloroaniline (2,6-DCA) were added to a 20 mM solution of the $[Ni(P^{Cy}_2N^{Bn}_2)_2]^{2+}$. After purging with H_2, as described above, spectra were acquired immediately and again at varying time points for 70 h.

NMR spectroscopy samples for protonation studies of $[Ni^0(P^{Cy}_2N^{Bn}_2)_2]$ or $[HNi(P^{Cy}_2N^{Bn}_2)_2]^+$ were prepared by dissolving ~10−20 mg of complex in 0.7−1.0 mL of solvent in an NMR tube. An atmosphere of H_2 was added to the headspace to retard the H_2 elimination pathway. The solution was then cooled (−40 °C) and equilibrated for at least 30 min. Dimethylformamide triflate [(DMF)-H](OTf) or 2,6-dichloroanilinium tetrafluoroborate ([(2,6-DCA)H]-(BF_4)) (1 or 2 equivalents from stock solutions) were added to the cooled NMR samples in volumes no greater than 20 μL via gastight syringe.

NMR Spectroscopy Experiments. A 300 MHz ^1H frequency Varian VNMRS system equipped with a direct detect dual band probe was used for one-dimensional studies. Two-dimensional studies utilized a 500 MHz ^1H frequency Varian VNMRS system with a Varian OneNMR probe. Typical 90° pulses were ~9 μs for ^1H and ~12 μs for ^{31}P. $^{31}P\{^1H\}$ NMR spectra were collected with waltz ^1H decoupling. The temperature was controlled from −40 °C to +25 °C using an XRII852 Sample Cooler (FTS Systems, Stone Ridge, NY) FTS chiller system.

Two-dimensional EXSY experiments were recorded using a standard phase-sensitive VNMRJ 2D NOESY pulse program with 128−256 increments, 16−64 scans per increment, and 0−200 ms mixing times. Short mixing times allowed for the observation of the first step of the exchange processes. A maximum of 100 ms mixing times were used for rate determinations to limit the loss of crosspeak intensity due to T_1 relaxation. The rates of intermolecular exchange were determined by $^{31}P\{^1H\}$ EXSY using EXSYCalc software (Mestrelab Research) incorporating methods developed by Perrin,[19] where the integrated crosspeak intensities at a given mixing time are

dx.doi.org/10.1021/ja307413x | J. Am. Chem. Soc. 2012, 134, 19409−19424

compared to the diagonal crosspeaks at a minimal mixing time to give pseudo first-order rates constants with respect to the isomer concentration. Exchanges rates were obtained using a three-site exchange model based on the number of crosspeaks observed in the spectrum for the **e**/**x** ⇆ **NiH**, **e**/**e** ⇆ **NiH**, and/or the **e**/**x** ⇆ **e**/**e** exchange processes. The pseudo first-order rate constants obtained were then converted to second-order rate constants based on the proposed rate equations for the forward and reverse reactions. For the **e**/**x** isomer, there are two ^{31}P resonances, where the **e**/**e** isomer and the **NiH** intermediate only have a single resonance. As a result, the rate constants determined by the EXSYcalc fitting process for the **e**/**x** isomer were then adjusted by a factor of 2 to compensate for the resonance intensity difference. Each experiment was repeated in triplicate.

Computational Details. *General strategy.* The computational study of the interconversion dynamics between the three isomers requires the modeling of (intermolecular) protonation and deprotonation steps, intramolecular proton transfers and chair/boar conformational changes. Intramolecular proton transfers and conformational changes can be easily described using standard quantum chemistry methodologies based on a stationary points search on the potential energy surface. In previous publications,[6,12c,28] we have shown that these calculations, complemented by harmonic thermal and entropic corrections along with a continuum description of the solvent, are adequately accurate and are employed in the present investigation to describe these processes. In contrast, the modeling of the acid/base reactions required for the intermolecular protonation/deprotonation steps cannot be easily modeled within standard quantum chemistry computational framework. The major problems encountered regard the calculation of (1) the entropic contribution to the reaction free energy and (2) the activation free-energy barrier. Indeed, the complex solvation/desolvation processes underlying the intermolecular protonation and deprotonation steps cannot be easily captured by a stationary point search on the PES of the reacting system (acid/base and the Ni complex) with a continuum description of the solvent. The inclusion of a few explicit molecules of the solvent is still problematic, as the number of molecules needed to correctly describe these processes is not known *a priori*. Instead, molecular dynamics simulations represent a consolidated tool to explore, at finite temperature, the complex interplay between solvent, acid/base and Ni complex.[29] Therefore, protonation/deprotonation steps were explored via hybrid quantum mechanics/molecular dynamics (QM/MM) simulations along with enhanced sampling techniques for free energy calculations.[30] These simulations are computationally demanding and cannot be applied to the study of all of the possible intermolecular processes involved in the isomerization. Rather, they were performed on selected reactions and the results extended to the other processes as discussed below.

QM/MM Simulations. The binding and dissociation free energies and activation free energies of aniline and the conjugate acid to the Ni-catalyst were calculated via *ab initio* QM/MM Born−Oppenheimer metadynamics molecular dynamics simulations.[31] The Ni catalyst and aniline or anilinium were treated at the QM level, whereas the solvent was described using the empirical potential by Nikitin and Lyubartsev.[32] The simulations were performed in the density functional theory (DFT) framework using the PBE functional level,[33] augmented with Grimme's correction for the dispersion energy (PBE+D2).[34] The van der Waals interaction between the QM atoms and the solvent was calculated using Lennard-Jones potentials. For the QM atoms, Lennard-Jones parameters were taken from Rappe et al.[35] for Ni(II) from the general amber force field (GAFF) database[36] for all of the remaining atoms. The QM/MM simulations were performed using the CP2K package.[37]

The metadynamics technique[31b,c] was employed to obtain the free energy profile for the binding and dissociation of aniline and anilinium as well the intermolecular proton transfer steps. Metadynamics is an adaptive biasing potential technique, which disfavors configurations that have been already explored, and consequently favors situations that would have been poorly explored thermally. The bias can be applied to any physical quantity describing the process being studied. To increase the sampling efficiency, a variant of metadynamics called multiple-walker metadynamics[31b] has been employed,[38] where 20 replicas of the system ("walkers") are propagated in time all contributing to the exploration of the free energy surface defined by a given set of collective variables. The collective variables employed are as follows. To investigate the binding of aniline to the Ni catalyst and the subsequent deprotonation step, we chose the distance between the N atom of aniline and the Ni center (RC_1) and the coordination number of the N atom of aniline to the H atoms of the protonated pendant amines (RC_2).[39] The isomerization requires chair/boat interconversion of the six-membered ring formed by the ligands and the metal center. This interconversion was followed by biasing the coordinate $RC_3 = \chi = (\phi_1\text{-}\phi_2\text{+}\phi_3\text{-}\phi_4\text{+}\phi_5\text{-}\phi_6)$ where ϕ_i are the internal torsional angles of a six member ring as described in ref 40. Gaussian functions of 0.1 kcal/mol in height and with a width of 0.1 Å for RC_1, 0.05 for RC_2 and 0.2 rad for RC_3 were employed to bias the phase space.

The starting configurations for the QM/MM multiple-walker metadynamics simulations were prepared as follows: (1) The Ni complex and aniline (anilinium) association complex in its gas-phase equilibrium geometry was solvated by more than 900 acetonitrile solvent molecules in a cubic box. The solvent was equilibrated at a constant pressure (p = 1 bar)[41] and a constant temperature (T = 300 K)[42] for 2 ns. (2) A constant volume, constant temperature simulation was run at the equilibrium density of the solution as obtained from the previous simulation. In these simulations, the catalyst and aniline (anilinium) were kept frozen in their DFT optimized structure in the gas phase. Point charges calculated according to the Amber RESP procedure were employed to describe the electrostatic interaction between catalysts and solvent. (3) Twenty uncorrelated configurations from the previous run were relaxed at QM/MM and then (4) each system was further equilibrated at 300 K by a 2 ps constant volume and constant temperature QM/MM simulation. The final configuration of each one of these runs was employed for the metadynamics simulations. The randomization of the solvent before step 3 is extremely important for a statistically meaningful exploration of the free energy landscape. In the metadynamics simulations Gaussian functions were added every 5 fs. The total simulation time ranged from 3.3 to 13 ps per replica, depending on the process investigated.

Standard Quantum Chemistry Calculations. The structure and thermodynamic properties of important intermediate states deriving from intramolecular processes were calculated by using standard quantum chemistry methodologies as discussed above. These calculations were performed using the PBE functional and are indicated as QM in the text. The Stuttgart basis set with effective core potential (ECP) was employed for the Ni atom,[43] and 6-31G* for all nonmetal atoms with additional p polarization functions on the protic or hydridic hydrogens.[44] This computational set up has been shown to describe the Ni-based H_2 chemistry with semiquantitative accuracy compared to coupled cluster CCSD(T) calculations.[28] Harmonic vibrational frequencies were calculated at the optimized structures using the same level of theory to estimate the zero-point energy (ZPE) and thermal contributions (T = 298K and p = 1 bar) to the gas-phase free energy. Solvation free energies were then computed using a self-consistent reaction field model at the same level of theory as for the other steps. The Continuum Polarizable Conductor Model (CPCM)[45] was used with Bondi radii.[46] These calculations were carried out with Gaussian 09.[47]

Analysis of the Binding Energy between Aniline or Anilinium and the Nickel Complex. To better understand the origin of the barrier for the association and dissociation of aniline and anilinium, the binding energy (ΔE_{bind}) between the aniline or anilinium and the corresponding Ni complex (e.g., the **e**/**x** isomer for the binding of aniline and the **NiH** intermediate for the binding of anilinium) as a function of the relative distance r was decomposed into two major contributions as defined in eq 3.

$$\Delta E_{bind} = \Delta E_{dis} + \Delta E_{int\text{-}sol} \quad (3)$$

In eq 3, ΔE_{dis} is the energy necessary to distort the nickel complex from the unbound geometry to the geometry at a close distance r;

$\Delta E_{int\text{-}sol}$ is the interaction energy between the electronic charge distributions of the two species in solution.

The term ΔE_{dis} quantifies the cost for "pre-organizing" the Ni catalyst for binding with the base and it is associated to the accessibility of the pendant amine (steric hindrance). It can be easily estimated from the energy difference between the isolated species at the equilibrium geometry in the association complex at a distance r and the equilibrium geometry in the bulk. The second term ($\Delta E_{int\text{-}sol}$) is mostly due to hydrogen bonding and the electrostatic interactions between the two species, the former being predominant at short distances. It can be estimated as the total energy for the complex plus aniline or anilinium at distance r minus ΔE_{dis}. These two contributions have been calculated at the QM level with a continuum description of the solvent. Anilinium is not a stable species in the association complex and a spontaneous proton transfer occurs as it has been discussed in the text. The association complex can be stabilized via hydrogen bonding by adding explicit solvent molecules around the anilinium. Since we are interested in the binding and unbinding energy of anilinium and not in the energy associated with the intermolecular proton transfer (which is reliably estimated from the metadynamics simulation), in this analysis of ΔE_{bind} the acetonitrile is removed and the N−H bond distances of the -NH_3^+ group have been constrained to the equilibrium value in the complex.

Although in the decomposition outlined above the conformational entropy of the system, binding/unbinding entropy, and the atomic detail of the solvent are neglected, the activation binding energies calculated according to eq 3 are consistent with the corresponding free energies calculated from the more accurate metadynamics simulations, with differences no higher than 6 kcal/mol. For instance, the barrier for the binding (dissociation) of aniline to (from) the endo position is 12 kcal/mol (3 kcal/mol) according to eq 3 and 7 kcal/mol (1 kcal/mol) from the metadynamics. Similarly, the activation energy for the binding (dissociation) of anilinium to (from) the endo position of the **NiH** intermediate is 21 kcal/mol (8 kcal/mol) according to eq 1 and 17 kcal/mol (9 kcal/mol) from the metadynamics. In the case of anilinium the dissociation free energies corresponds to the quantity $\Delta G^{\ddagger}_{d,diss}$ defined earlier (See Figure 11). Similar qualitative agreement is found for binding to the exo position.

■ ASSOCIATED CONTENT

Ⓢ Supporting Information

NMR spectra for the protonation of $[Ni^0(P^{Cy}_2N^{Bn}_2)_2]$ in butyronitrile; NMR spectra for the protonation of $[Ni^0(P^{Cy}_2N^{Bn}_2)_2]$ by $[(DMF)H]^+$; NMR spectra for the protonation of $[HNi(P^{Cy}_2N^{Bn}_2)_2]^+$; Comparison of isomer equilibration times with different additives; Isomer distribution under different solution conditions; ^1H EXSY of $[Ni(P^{Cy}_2N^{Bn}_2)_2]^{2+}$; Plot of dependence of the equilibration rate on the concentration of aniline; ^{31}P EXSY with no added aniline; The free energy surface of the dissociation of anilinium from **B:e/NiH** species; The free energy surface of the dissociation of anilnium from **B:e/e** species; Free energy diagram of the chair/boat interconversion in $Ni(P^{Cy}_2N^{Me}_2H)_2^{2+}$ with and without aniline hydrogen-bonded to the exo proton; Free energy landscape for the binding of aniline to the exo position of the **e/x** isomer as a function of the chair/boat conformation of the nonprotonated ring of the pinched structure; Free energy diagram for the **e/e** ⇆ **NiH** alternative interconversion mechanisms catalyzed by aniline; Complete citation for ref 47. This material is available free of charge via the Internet at http://pubs.acs.org.

■ AUTHOR INFORMATION

Corresponding Author

simone.raugei@pnnl.gov; wendy.shaw@pnnl.gov

Notes

The authors declare no competing financial interest.

■ ACKNOWLEDGMENTS

We thank Dr. Michel Dupuis, Dr. Roger J. Rousseau, Dr. Shentan Chen, and Dr. John Linehan for useful discussions. This research was carried out in the Center for Molecular Electrocatalysis, an Energy Frontier Research Center funded by the U.S. Department of Energy, Office of Science. W.J.S. was funded by the DOE Office of Science Early Career Research Program through the Office of Basic Energy Sciences. Pacific Northwest National Laboratory is operated for the U.S. Department of Energy by Battelle. Computational resources were provided at W. R. Wiley Environmental Molecular Science Laboratory (EMSL), a national scientific user facility sponsored by the Department of Energy's Office of Biological and Environmental Research located at Pacific Northwest National Laboratory, the National Energy Research Scientific Computing Center (NERSC) at Lawrence Berkeley National Laboratory, and the Jaguar supercomputer at Oak Ridge National Laboratory (INCITE 2008-2011 award supported by the Office of Science of the U.S. DOE under Contract No. DE-AC0500OR22725).

■ REFERENCES

(1) (a) Fontecilla-Camps, J. C.; Volbeda, A.; Cavazza, C.; Nicolet, Y. *Chem. Rev.* **2007**, *107*, 4273−4303. (b) Guskov, A.; Kern, J.; Gabdulkhakov, A.; Broser, M.; Zouni, A.; Saenger, W. *Nat. Struct. Mol. Biol.* **2009**, *16*, 334−342. (c) Konstantinov, A. A.; Siletsky, S.; Mitchell, D.; Kaulen, A.; Gennis, R. B. *Proc. Natl. Acad. Sci. U.S.A.* **1997**, *94*, 9085−9090.

(2) Cukierman, S. *Biochim. Biophys. Acta, Bioenerg.* **2006**, *1757*, 876−885.

(3) Nicolet, Y.; de Lacey, A. L.; Vernede, X.; Fernandez, V. M.; Hatchikian, E. C.; Fontecilla-Camps, J. C. *J. Am. Chem. Soc.* **2001**, *123*, 1596−1601.

(4) (a) DuBois, D. L.; Bullock, R. M. *Eur. J. Inorg. Chem.* **2011**, 1017−1027. (b) Ott, S.; Kritikos, M.; Åkermark, B.; Sun, L.; Lomoth, R. *Angew. Chem., Int. Ed.* **2004**, *43*, 1006−1009. (c) Gloaguen, F.; Rauchfuss, T. B. *Chem. Soc. Rev.* **2009**, *38*, 100−108. (d) Sun, L.; Åkermark, B.; Ott, S. *Coord. Chem. Rev.* **2005**, *249*, 1653−1663.

(5) (a) Kilgore, U.; Roberts, J.; Pool, D. H.; Appel, A.; Stewart, M.; Rakowski DuBois, M.; Dougherty, W. G.; Kassel, W. S.; Bullock, R. M.; DuBois, D. L. *J. Am. Chem. Soc.* **2011**, *133*, 5861−5872. (b) Helm, M. L.; Stewart, M. P.; Bullock, R. M.; Rakowski DuBois, M.; DuBois, D. L. *Science* **2011**, *333*, 863−866. (c) Wiese, S.; Kilgore, U. J.; DuBois, D. L.; Bullock, R. M. *ACS Catal.* **2012**, *2*, 720−727.

(6) Yang, J. Y.; Chen, S.; Dougherty, W. G.; Kassel, W. S.; Bullock, R. M.; DuBois, D. L.; Raugei, S.; Rousseau, R.; Dupuis, M.; Rakowski DuBois, M. *Chem. Commun.* **2010**, *46*, 8618−8620.

(7) Smith, S. E.; Yang, J. Y.; DuBois, D. L.; Bullock, R. M. *Angew. Chem.* **2012**, *124*, 3206−3209.

(8) Le Goff, A.; Artero, V.; Jousselme, B.; Tran, P. D.; Guillet, N.; Métayé, R.; Fihri, A.; Palacin, S.; Fontecave. *Science* **2009**, *326*, 1384−1387.

(9) Jain, A.; Lense, S.; Linehan, J. C.; Raugei, S.; Cho, H.; DuBois, D. L.; Shaw, W. J. *Inorg. Chem.* **2011**, *50*, 4073−4085.

(10) Yang, J. Y. Unpublished results.

(11) Wilson, A. D.; Shoemaker, R. K.; Miedaner, A.; Muckerman, J. T.; DuBois, D. L.; Rakowski DuBois, M. *Proc. Natl. Acad. Sci. U.S.A.* **2007**, *104*, 6951−6956.

(12) (a) Dupuis, M.; Chen, S.; Raugei, S.; DuBois, D. L.; Bullock, R. M. *J. Phys. Chem. A* **2011**, *115*, 4861−4865. (b) Raugei, S.; Chen, S.; Ho, M.-H.; Ginovska-Pangovska, B.; Rousseau, R. J.; Dupuis, M.; DuBois, D. L.; Bullock, R. M. *Chem.—Eur. J.* **2012**, *18*, 6493−6506. (c) O'Hagan, M.; Shaw, W. J.; Raugei, S.; Chen, S.; Yang, J. Y.; Kilgore,

U. J.; DuBois, D. L.; Bullock, R. M. *J. Am. Chem. Soc.* **2011**, *133*, 14301−14312.
(13) Appel, A. M.; Pool, D. H.; O'Hagan, M.; Shaw, W. J.; Yang, J. Y.; Rakowski DuBois, M.; DuBois, D. L.; Bullock, R. M. *ACS Catal.* **2011**, *1*, 777−785.
(14) Wilson, A. D.; Newell, R. H.; McNevin, M. J.; Muckerman, J. T.; Rakowski DuBois, M.; DuBois, D. L. *J. Am. Chem. Soc.* **2006**, *128*, 358−366.
(15) Wiedner, E. S.; Yang, J. Y.; Chen, S.; Raugei, S.; Dougherty, W. G.; Kassel, W. S.; Helm, M. L.; Bullock, R. M.; Rakowski DuBois, M.; DuBois, D. L. *Organometallics* **2011**, *31*, 144−156.
(16) (a) Kaljurand, I.; Kutt, A.; Soovali, L.; Rodima, T.; Maemets, V.; Leito, I.; Koppel, I. A. *J. Org. Chem.* **2005**, *70*, 1019−1028. (b) Izutsu, K. *Acid-Base Dissociation Constants in Dipolar Aprotic Solvents*; Blackwell Scientific Publications: Oxford, 1990. (c) Kolthoff, I. M.; Chantooni, M. K., Jr.; Bhowmik, S. *Anal. Chem.* **1967**, *39*, 1627−1633.
(17) A small amount of the **x**/**x** isomer was observed due to a Ni(0) impurity.
(18) The rate of isomerization is very sensitive to catalyst concentration and temperature as well, and consequently, these were carefully controlled.
(19) Perrin, C. L.; Dwyer, T. J. *Chem. Rev.* **1990**, *90*, 935−967.
(20) Fraze, K.; Wilson, A. D.; Appel, A. M.; Rakowski DuBois, M.; DuBois, D. L. *Organometallics* **2007**, *26*, 3918−3924.
(21) The pK_a's of the pendant amine for the various species involved in the isomerization process were calculated using an isodesmic scheme where anilinium/aniline was chosen as a reference system in this study.
(22) Chen, S.; Rousseau, R.; Raugei, S.; Dupuis, M.; DuBois, D. L.; Bullock, R. M. *Organometallics* **2011**, *30*, 6108−6118.
(23) Pinter, B.; Fievez, T.; Bickelhaupt, F. M.; Geerlings, P.; De Proft, F. *Phys. Chem. Chem. Phys.* **2012**, *14*, 9846−9854.
(24) Appel, A. M.; Pool, D. H.; O'Hagan, M.; Shaw, W. J.; Yang, J. Y.; Rakowski DuBois, M.; DuBois, D. L.; Bullock, R. M. *ACS Catal.* **2011**, *1*, 777−785.
(25) Kilgore, U. J.; Stewart, M. P.; Helm, M. L.; Dougherty, W. G.; Kassel, W. S.; DuBois, M. R.; DuBois, D. L.; Bullock, R. M. *Inorg. Chem.* **2011**, *50*, 10908−10918.
(26) Camara, J. M.; Rauchfuss, T. B. *J. Am. Chem. Soc.* **2011**, *133*, 8098−8101.
(27) Kaljurand, I.; Kutt, A.; Soovali, L.; Rodima, T.; Maemets, V.; Leito, I.; Koppel, I. A. *J. Org. Chem.* **2005**, *70*, 1019−1028.
(28) Chen, S.; Raugei, S.; Rousseau, R.; Dupuis, M.; Bullock, R. M. *J. Phys. Chem. A* **2010**, *114*, 12716−12724.
(29) Ivanov, I.; Chen, B.; Raugei, S.; Klein, M. L. *J. Phys. Chem. B* **2006**, *110*, 6365−6371.
(30) Laio, A.; Gervasio, F. L. *Rep. Prog. Phys.* **2008**, *71*, 126601.
(31) (a) Laino, T.; Mohamed, F.; Laio, A.; Parrinello, M. *J. Chem. Theory Comput.* **2006**, *2*, 1370−1378. (b) Laio, A.; Gervasio, F. L. *Rep. Prog. Phys.* **2008**, *71*, 126601. (c) Laio, A.; Parrinello, M. *Proc. Natl. Acad. Sci. U.S.A.* **2002**, *99*, 12562−12566.
(32) Nikitin, A. M.; Lyubartsev, A. P. *J. Comput. Chem.* **2007**, *28*, 2020−2026.
(33) (a) Perdew, J. P.; Burke, K.; Ernzerhof, M. *Phys. Rev. Lett.* **1997**, *78*, 1396−1396. (b) Perdew, J. P.; Burke, K.; Ernzerhof, M. *Phys. Rev. Lett.* **1996**, *77*, 3865−3868.
(34) Grimme, S. *J. Comput. Chem.* **2006**, *27*, 1787−1799.
(35) Rappe, A. K.; Casewit, C. J.; Colwell, K. S.; Goddard, W. A., III; Skiff, W. M. *J. Am. Chem. Soc.* **1992**, *114*, 10024−10035.
(36) Wang, J.; Wolf, R. M.; Caldwell, J. W.; Kollman, P. A.; Case, D. A. *J. Comput. Chem.* **2004**, *25*, 1157−1174.
(37) VandeVondele, J.; Krack, M.; Mohamed, F.; Parrinello, M.; Chassaing, T.; Hutter, J. *Comput. Phys. Commun.* **2005**, *167*, 103−128.
(38) Raiteri, P.; Laio, A.; Gervasio, F. L.; Micheletti, C.; Parrinello, M. *J. Phys. Chem. B* **2005**, *110*, 3533−3539.
(39) Iannuzzi, M.; Laio, A.; Parrinello, M. *Phys. Rev. Lett.* **2003**, *90*, 238302.
(40) Ionescu, A. R.; Bérces, A.; Zgierski, M. Z.; Whitfield, D. M.; Nukada, T. *J. Phys. Chem. A* **2005**, *109*, 8096−8105.
(41) Parrinello, M.; Rahman, A. *J. Appl. Phys.* **1981**, *52*, 7182−7190.
(42) Martyna, G. J.; Klein, M. L.; Tuckerman, M. *J. Chem. Phys.* **1992**, *97*, 2635−2643.
(43) Andrae, D.; Häußermann, U.; Dolg, M.; Stoll, H.; Preuß, H. *Theor. Chem. Acc.* **1990**, *77*, 123−141.
(44) Rassolov, V. A.; Pople, J. A.; Ratner, M. A.; Windus, T. L. *J. Chem. Phys.* **1998**, *109*, 1223−1229.
(45) (a) Barone, V.; Cossi, M. *J. Phys. Chem. A* **1998**, *102*, 1995−2001. (b) Cossi, M.; Rega, N.; Scalmani, G.; Barone, V. *J. Comput. Chem.* **2003**, *24*, 669−681.
(46) Bondi, A. *J. Phys. Chem.* **1964**, *68*, 441−451.
(47) Frisch, M. J.; et al. *Gaussian 09*; Gaussian, Inc.: Wallingford, CT, 2009.